Biomaterials Science

PAPER

View Article Online
View Journal | View Issue

Cite this: *Biomater. Sci.*, 2026, **14**, 547

Electrically conductive and mechanoactive scaffolds synergistically enhance osteogenic cell responses under mechanical stimulation

Nikoleta N. Tavernaraki, [a] Varvara Platania, [a] Kalliopi Alpantaki, [b] Nikoletta Triantopoulou, [c] Marina Vidaki, [c,d] Massimiliano Labardi, [e] Serena Danti [e,f] and Maria Chatzinikolaidou *[a,g]

Bone is a dynamic tissue that responds to mechanical forces and possesses intrinsic mechanoelectrical activity. Recently, electrically conductive polymers have emerged as stimulating biomaterials for bone tissue engineering. However, the effect of conductive scaffolds under mechanical stimulation towards bone formation remains unclear. This study presents the development of electrically conductive, mechanoactive porous scaffolds, and the validation of their osteogenic capacity under mechanical stimulation. The developed scaffolds contain poly(3,4-ethylenedioxythiophene) polystyrene sulfonate (PEDOT:PSS) into a double polymeric network comprising poly(vinyl alcohol) (PVA) and gelatin (Gel). PEDOT-containing scaffolds demonstrated superior electrical conductivity, increased surface porosity, and an elevated Young modulus of 2.7 ± 0.4 MPa compared to the PVA/Gel control. Pre-osteoblastic cells cultured within the conductive, mechanoactive scaffolds under uniaxial compression showed increased cell viability, calcium influx, and upregulation of osteogenic markers. Mechanical loading enhanced the activation of the mechanotransduction markers YAP/TAZ, upregulated alkaline phosphatase activity, collagen secretion, and calcium deposition, particularly in PEDOT-containing scaffolds, with hydroxyapatite formation on day 21. *In vivo* subcutaneous implantation of the developed scaffolds indicated lack of any adverse immune responses. These results highlight the great potential of the developed electroactive, mechanoresponsive scaffolds as biomimetic substrates to enhance osteogenesis under mechanical stimulation.

Received 12th July 2025,
Accepted 30th November 2025

DOI: 10.1039/d5bm01064k

rsc.li/biomaterials-science

1. Introduction

Autologous bone grafting is currently regarded as the gold standard for treating critical bone defects. However, this approach has limitations, including the scarcity of available autografts, potential donor site complications, such as infection, chronic pain, and the risk of graft failure.[1] Bone tissue engineering (BTE) has emerged as a promising therapeutic strategy, by introducing platforms mimicking the key components of autografts through three main elements, the biomaterial scaffolds, the bioactive molecules, and stem cells.[2] Bioactive molecules, often in the form of recombinant growth factors[3] or bioactive small peptides provide osteoinductive properties.[4] However, their use poses challenges, including an initial burst release, reduced biological activity over time, the need for high therapeutic doses, and potential side effects.[5] To overcome these limitations, there is a strong need to incorporate additional components with osteoinductive properties for BTE to enhance bone regeneration and healing. To this purpose, biophysical stimuli have recently attracted great attention for bone regeneration.

Bone tissue is characterized by its dynamic nature and constant exposure to mechanical forces throughout life, exhibiting high responsiveness to such stimuli.[6] Since 1892, Wolff postulated that bone is a mechanosensitive tissue, which forms and constantly remodels by adapting to the mechanical forces applied on it.[7] Additionally, the discovery of the mechanoelectrical properties of bone dates back to the 1950s, when Fukada and Yasuda found that applying mechanical stress to bone in various directions generated electrical signals. These signals

[a]*Department of Materials Science and Engineering, University of Crete, Heraklion, Greece. E-mail: mchatzin@uoc.gr*
[b]*Department of Orthopedics and Trauma, Venizeleion General Hospital, Heraklion, Greece*
[c]*Department of Basic Science, Faculty of Medicine, University of Crete, Heraklion, Greece*
[d]*Institute of Molecular Biology and Biotechnology, Foundation for Research and Technology Hellas, Heraklion, Greece*
[e]*CNR-IPCF, Sede Secondaria di Pisa, Pisa, Italy*
[f]*Department of Civil and Industrial Engineering, University of Pisa, Pisa, Italy*
[g]*Institute of Electronic Structure and Laser, Foundation for Research and Technology-Hellas, Heraklion, Greece*

created an endogenous electric field that promoted the proliferation of osteogenic cells.[8] Since then, research has indicated that stress on the bony crystalline structure induces electrical currents, aiding in healing.[9] This endogenous electric field arises as mechanical load on the bone tissue creating strain gradients, leading to pressure gradients, which in turn drive interstitial fluid through small channels, called canaliculi, within the bone. As this fluid flows from compressed regions to areas under tension, electrical potentials are generated.[9] When bone tissue is injured, the physiological mechanoelectrical microenvironment at the fracture site is distorted, which blocks the mechanical forces and the electric charge transfer across the fracture to delay the healing process.[10] Along with fixing the mechanical continuity of the tissue, the reconstruction of the local electrical microenvironment at the bone defect site provides an effective strategy to promote bone regeneration. Hence, the application of electroactive biomaterials to fill the defect area can facilitate localized electrical stimulation, thus enhancing bone regeneration.[11] Poly(3,4-ethylenedioxythiophene) (PEDOT) is a conductive polymer,[12,13] which, in combination with polystyrene sulfonate (PSS), that improves its water solubility, has been described as a promising material for biomedical applications. PEDOT:PSS serves as an optimal substrate for supporting the growth and electrical stimulation of various cell types, particularly osteogenic cells,[12,14] while it has been reported to enhance the mechanical properties of scaffolds, making them favorable for BTE applications.[15]

BTE scaffolds act as templates for cells and growth factors to mimic the extracellular matrix (ECM) of bone, maintain and restore bone tissue function. High porosity, pore interconnectivity, biocompatibility, biodegradability, and mechanical properties are indispensable properties to be considered when designing scaffolds for cancellous bone. Gelatin (Gel) is a natural biomaterial, produced through the partial denaturation of collagen.[16] Its inherent ability to mimic the biochemical and mechanical cues of native cancellous bone ECM facilitates enhanced cell-scaffold interactions ensuring minimal immune response after implantation. Moreover, gelatin exhibits excellent biodegradability, allowing for gradual scaffold degradation, coinciding with new tissue formation.[17] Polyvinyl alcohol (PVA) is a synthetic polymer approved by the Food and Drug Administration (FDA) and serves as an alternative for polar, water-soluble materials,[18] it is flexible and unique among synthetic polymers for its hydrophilicity due to the many hydroxyl groups. The extent of its biodegradability depends on its molecular weight and degree of hydrolysis, which are crucial factors for its suitability in biological applications. Furthermore, PVA blended with other biopolymers has shown to enhance cellular attachment and proliferation,[19] also facilitating a conducive environment for osteogenic differentiation and mineralization, enabling the formation of functional bone tissue.[20]

Compression bioreactors aim to replicate the *in vivo* environment by applying mechanical stress to cells within an *in vitro* setting. The response to mechanical stimuli depends on both the intensity of the applied forces and the resulting strain. It has been reported that a displacement range between 50 μm and 1500 μm is associated with bone remodeling,[21] and when strain exceeds the upper limit, bone tissue responds by regrowing to counteract the local deformation, whereas below the lower threshold, bone resorption becomes more dominant. Research reports have indicated that the number of cycles and strain level impact the proliferation of human osteoblasts, while frequency changes affect the cell proliferation at a constant cycle count.[22] The authors reported on an optimal frequency for promoting cell proliferation at 1 Hz, while they found that uniaxial and biaxial strain can enhance osteoblast proliferation and differentiation, though the biochemical mechanisms underlying these processes are not yet fully understood.

Recent studies reported on electroactive PEDOT:PSS porous scaffolds[12] and polyacrylonitrile (PAN)/PEDOT:PSS electrospun membranes as mineralized scaffolds for bone tissue engineering.[23] Although electroactive polymers have been used as scaffolds to enhance osteogenic responses in the presence of electrical stimulation,[24] the effect of conductive PEDOT:PSS-containing scaffolds under mechanical stimulation towards bone formation still remains elusive. Our study fills this gap by investigating the effect of mechanical stimulation to generate electrical signals on pre-osteoblastic cells cultured on electrically conductive, mechanosensitive PEDOT:PSS-containing scaffolds. We hypothesized that mechanical stress applied to bone-forming cells, cultured on biomimetic electroactive PVA/Gel/PEDOT:PSS scaffolds, generates electrical signals, which ultimately produce an endogenous electric field that supports osteogenic cell responses. The developed scaffolds combine electroactive (electrical conductivity) properties, imparted by PEDOT:PSS, with mechanical stimulation, creating an environment that effectively mimics the native bone behavior. This electro-mechanic synergistic effect is evident through the results of the osteogenic experiments, where enhanced differentiation was observed only when both factors were present. To validate this, we included two critical controls, scaffolds without the conductive polymer, and scaffolds maintained under static conditions without mechanical stimulation. This experimental design allowed us to clearly attribute the observed osteogenic responses to the combined action of electrical conductivity and mechanical stimulation. Evidence of increased osteogenic differentiation potential under mechanical stimulation is exhibited through the assessment of osteogenic markers such as alkaline phosphatase activity, collagen and calcium production, matrix mineralization, and hydroxyapatite formation, as well as activity of voltage-gated calcium channels, and the mechanotransduction receptors yes-associated protein (YAP) and transcriptional coactivator with PDZ binding motif (TAZ).[25] Moreover, lack of any adverse immune reactions has been observed following *in vivo* subcutaneous implantation of the developed functional scaffolds for two weeks in mice. This study aims to advance bone regeneration strategies by investigating how mechanical forces and electroactivity may affect the osteogenic differentiation.

2. Materials and methods

2.1. Preparation of porous scaffolds comprising PVA, gelatin and PEDOT:PSS

Two different scaffold compositions were prepared, using (i) PVA/gelatin with a ratio of 5% w/v PVA and 5% w/v gelatin, which served as control scaffold, and (ii) 0.15% w/v PEDOT:PSS mixed with 5% w/v PVA and 5% w/v gelatin. PEDOT:PSS-containing scaffolds were prepared from a PEDOT:PSS stock dispersion of 1.3% w/v (Sigma-Aldrich, Schnelldorf, Germany). The exact composition of the two polymers in the dispersion was 0.5% w/v PEDOT and 0.8% w/v PSS diluted in water, with PSS making PEDOT soluble in water. The PEDOT:PSS concentration of 0.15% w/v was selected based on optimization experiments as it presented the highest concentration providing electroconductivity, while maintaining cytocompatibility (S1, S2). Higher concentrations, such as 0.3%, have been reported to impair cell viability and spreading due to the excess anionic PSS component.[26] All reagents were UV irradiated prior blending, ensuring that subsequent cell culture experiments were performed under sterile conditions and to eliminate the risk of microbial contamination. For the preparation of the PVA/gelatin blend, 5% w/v of PVA were dissolved in sterile deionized water and the solution was kept under stirring for 3 h at 90 °C, followed by the addition of gelatin under stirring at 60 °C for 1 h until homogeneous incorporation. The PVA/gelatin blend was combined with the PEDOT:PSS dispersion to achieve a final concentration of 0.15% w/v in the blend. Prior blending, the stirring temperature was decreased to room temperature (RT) and PEDOT:PSS was exposed to UV and sonicated. The final solution was kept under stirring for 3 h at RT, and then casted into each well of a 96 well-plate. Four freezing/thawing cycles of 24 h each were conducted, as subjecting conductive polymers to repeated freeze–thaw cycles has the potential to reshape their microstructure, leading in a substantial enhancement of the mechanical and electrochemical properties of the final product.[27] After four cycles, the hydrogels were freeze-dried for 45 min at −40 °C, kept under sterile conditions and crosslinked. The PEDOT:PSS-containing scaffolds were double-crosslinked with 2% v/v (3-glycidyloxypropyl) trimethoxysilane (GOPS)[12] and 0.025% v/v glutaraldehyde[28] for 15 min each, while the PVA/gelatin control scaffolds were crosslinked only by the latter. The crosslinkers were diluted in phosphate buffered saline (PBS). The scaffolds were then thoroughly rinsed with PBS in order to remove any unbound residues of crosslinker that might be cytotoxic during the biological evaluation. The fabrication protocol is displayed in the schematic (Fig. 1).

2.2. Physicochemical and mechanical characterization of the scaffolds

2.2.1. Fourier transform infrared (FTIR) and Raman spectroscopy. ATR-FTIR spectra analysis of the basic components, PEDOT:PSS, gelatin and PVA, as well as the fabricated scaffolds, was performed in transmittance mode using a Nicolet 6700 FT-IR spectrometer (Thermo Fisher Scientific Inc., Waltam, MA, USA). The instrument can be equipped with different sampling accessories. In our case, we used the Smart-

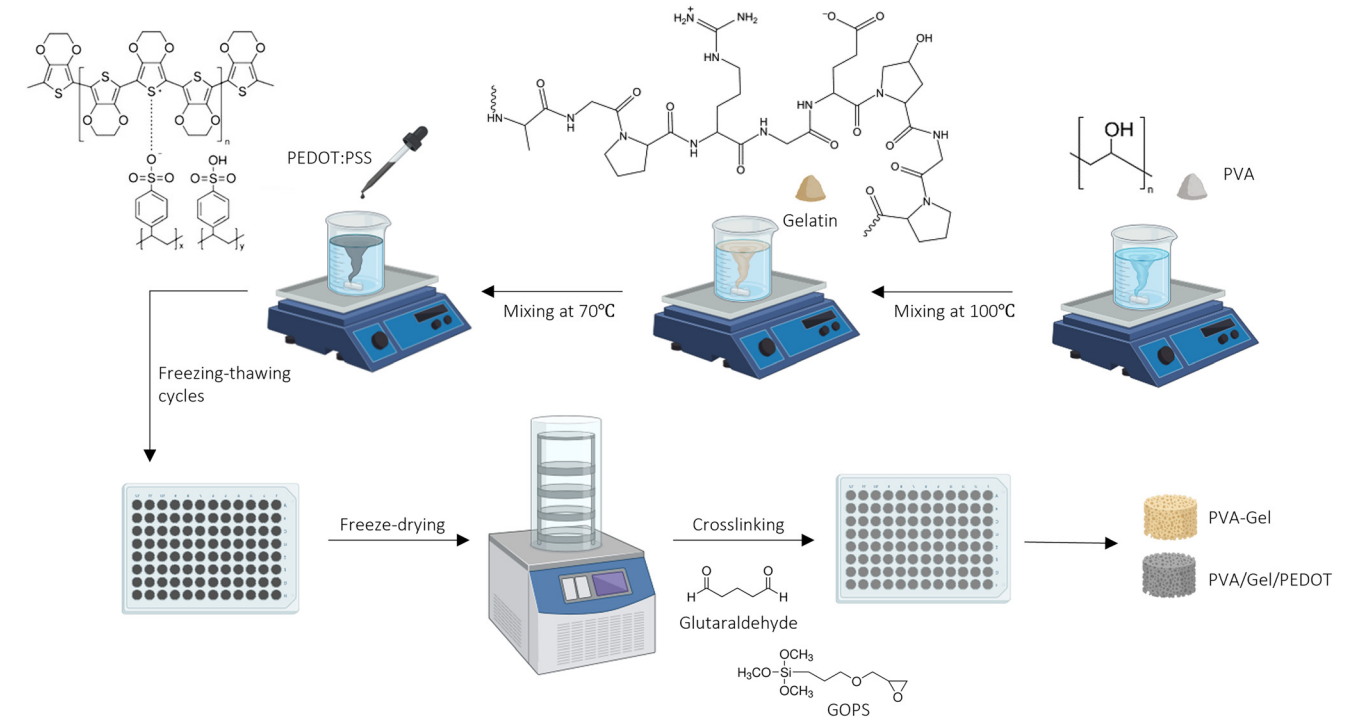

Fig. 1 Schematic (created with BioRender) on the workflow of the scaffold fabrication. PEDOT:PSS is the acronym for poly(3,4-ethylene dioxythiophene):poly(styrene sulfonate), PVA is the acronym for poly(vinyl)-alcohol, and GOPS is the acronym for (3-glycidyloxypropyl) trimethoxysilane.

iTR ATR (Attenuated Total Reflection) accessory to collect the spectra.[29] For each spectrum, 32 scans were collected in the range of 4000–500 cm^{-1}.

Raman spectroscopy was employed to further confirm the presence of PEDOT:PSS within the scaffold matrix, using a modified LabRAM HR Raman Spectrometer (HORIBA Scientific, Lille, France) equipped with a 532 nm excitation laser source (maximum power output 90 mW). A 50× × LMPlanFL N objective lens (Olympus, Tokyo, Japan) with a numerical aperture of 0.5 and a working distance of 2.1 mm was employed for delivering the excitation energy and to acquire images and returning Raman signal. A neutral density filter limited the excitation energy to 10%, providing a laser power of approximately 4 mW on the sample. The resulting laser spot size was about 1.3 μm in diameter and 1.6 μm in axial length. Spectra were collected using a 600 grooves per mm grating, achieving a spectral resolution of roughly 2 cm^{-1}. Signal detection was achieved through a Syncerity CCD Deep Cooled Camera (HORIBA) operating at −50 °C. Calibration was carried out using a SiO_2 reference (peak at 520.7 cm^{-1}). Raman spectra were acquired over the 300–1900 cm^{-1} range for PEDOT:PSS pure and over the 40–3050 cm^{-1} range for PVA/Gel/PEDOT scaffold, in 1 and 3 spectral windows respectively, with an acquisition time of 20 s per scan and 3 accumulations (total ∼60 s per point). Data processing included cosmic ray removal (LabSpec LS6 software, HORIBA).

2.2.2. Evaluation of degradation and dissolution rate. The coupled effect of matrix degradation and dissolution was investigated upon determination of % mass loss rates. Firstly, the scaffolds were weighed at day 0 and then allowed to incubate at 37 °C in PBS. The scaffolds were removed from the medium on day 4 and subsequently on days 7, 14, 21, and 28, thoroughly dried, and their weight was measured by means of a precision balance. Measurements were taken in seven replicates (n = 7) of each scaffold type. The degradation/dissolution rate at day i, D_i, was expressed as a percentage of weight loss of the biomaterial by the following formula:

$$D_i = \frac{w_{\text{day}-0} - w_{\text{day}-i}}{w_{\text{day}-0}} \times 100\%$$

where $w_{\text{day-0}}$ is the initial weight of the scaffolds and $w_{\text{day-}i}$ is the weight of the scaffolds at the respective days, starting at day 4.

2.2.3. Liquid uptake measurement. The swelling capability of the scaffolds was evaluated by weighting freeze-dried scaffolds and allowing them to soak in PBS for 24 h at 37 °C. Then, the scaffolds were removed from the buffer, drained with a paper towel, and weighed again. The liquid uptake ability (swelling ratio S) was expressed as a percentage of weight increase in the biomaterial (n = 7), by the following formula:

$$S = \frac{w_{\text{wet}} - w_{\text{dry}}}{w_{\text{dry}}} \times 100\%$$

where w_{wet} is the weight of the wet scaffolds and w_{dry} is the weight of the dry scaffolds.

2.2.4. Electrical conductivity of scaffolds. Conductivity measurements on hydrated scaffolds were performed as follows. Each scaffold was hydrated by immersion in bidistilled water for 60 min. A disc of swollen scaffold (8 mm diameter) was cut, and placed on a precision scale, until the weight of around 64 mg was reached due to water evaporation, while the disc thickness was checked to be still larger than 1 mm. After, the disc was fitted into the center of a sealed dielectric cell, composed of two gold-plated disk electrodes (12 mm diameter) spaced by a Teflon ring (1 mm thickness, 9 mm internal diameter), that were pressed until sealing. By this way, measurements were performed on a given volume of material, of about 64 mm^3, and with a given quantity of water swollen by the hydrogel. Complex impedance $\hat{Z}$ was measured by broadband dielectric spectroscopy (BDS) as a function of frequency, f, in the range from 10^{-2} Hz to 10^7 Hz, by an Alpha Analyzer spectrometer (Novocontrol technologies GmbH, Montabaur, Germany). Cell seal was checked by comparing the results of repeated ($n \geq 2$) measurements. The real part of the electrical conductivity (σ') was calculated by the relation:

$$\sigma' = Re\left(\frac{d}{A}\hat{Z}^{-1}\right)$$

where A is the area of the cell (64 mm^2) and d its thickness (1 mm).

2.2.5. Porosity. The porosity of the scaffolds was imaged *via* SEM micrographs and the surface porosity (%) was calculated using ImageJ software (version 1.54) ($5 < n < 7$). Cross sections were obtained from the different freeze-dried scaffold types following sputter-coating with a 20 nm thick layer of Au (Baltec SCD 050, Los Angeles, CA, USA), and observed under SEM (JEOL JSM-6390LV, Tokyo, Japan) at an accelerating voltage of 15 kV.

2.2.6. Mechanical characterization of the scaffolds. The effect of PEDOT:PSS incorporation into PVA/Gel on the hydrogels' mechanical properties was evaluated by uniaxial compression tests. The mechanical compression tests were performed by using a mechanical test system, (UniVert, CellScale, Waterloo, Canada) equipped with a 50 N sensor at RT. Cylindrical hydrogel samples with a diameter of 1 cm and approximately 2 cm high were employed. The measurements were performed in six replicates (n = 6) from each scaffold composition. Compression loading was performed at a 15 mm s^{-1} deformation speed of up to 100% strain. The Young's modulus of the samples was determined as the slope in the linear elastic deformation region of the stress–strain curves. Therefore Young modulus Y at 60–90% strain[30] was calculated using the following formula:

$$Y = \frac{F \times L}{A \times \Delta L}$$

where F stands for the uniaxial force applied to the surface of the scaffolds, A is the surface where the pressure is applied, ΔL is the deformation after the force application and L is the initial height of the sample.

2.3. Evaluation of cytotoxicity and cell adhesion of cell-loaded scaffolds

2.3.1. Cell culture maintenance. The MC3T3-E1 cells (ACC-210, Leibniz Institute DSMZ, Germany) were used as a model system for the *in vitro* investigation of the viability and proliferation in the presence of the PVA/gelatin/PEDOT:PSS scaffolds and PVA/gelatin control scaffolds. The cells were cultured in alpha-MEM™ (PAN-Biotech, Aidenbach, Germany) medium supplemented with 10% fetal bovine serum (FBS) (PAN-Biotech, Aidenbach, Germany), 2 mM L-glutamine (PAN-Biotech, Aidenbach, Germany), 100 μg ml^{-1} penicillin/streptomycin (PAN-Biotech, Aidenbach, Germany), and 2.5 μg ml^{-1} amphotericin (fungizone) (Thermo Fisher Scientific, Waltham, MA, UK), in a cell culture incubator (Thermo Fisher Scientific, Waltham, MA, UK) set at 37 °C under a 5% CO_2 air humidified environment. After reaching 80–90% confluence, the cells were harvested using trypsin/EDTA (Thermo Fisher Scientific, Waltham, MA, UK). Specifically, 5×10^3 cells were seeded onto the scaffolds and were used for both viability and proliferation assays. The medium was replaced every three days. All experiments were carried out using cells at passages 6–8. A timeline of the viability experiments, for better visual understanding, and a more complete description of the experimental steps taken and timepoints chosen, is depicted in Fig. 2.

2.3.2. Evaluation of the scaffolds' cytocompatibility using a metabolic assay. The cellular viability was determined by means of the resazurin-based PrestoBlue™ assay. At each experimental time point (days 1, 3 and 7) during the culture, PrestoBlue™ reagent diluted in alpha-MEM™ at a volume ratio of 1 : 10 was added to each well at 10 μl per sample and incubated at 37 °C for 60 min. The supernatants, 100 μl/sample, were transferred to a 96-well plate, and the absorbance was measured at 570 and 600 nm using a spectrophotometer (Synergy HTX Multi-Mode Microplate Reader, BioTek, Bad Friedrichshall, Germany). All samples were rinsed with PBS, and thereafter, fresh culture medium was added. The cell metabolic activity was correlated with cell numbers by means of a calibration curve. All samples were analyzed using eight replicates ($n = 8$).

2.3.3. Pre-osteoblastic cell morphology and adhesion. Immunofluorescent staining of the cytoskeleton using TRITC-conjugated phalloidin (540 nm excitation/565 nm emission) (Sigma-Aldrich, Schnelldorf, Germany) and cell nuclei using 4′,6-diamidino-2-phenylindole (DAPI) (350 nm excitation/465 nm emission) (ThermoFisher Scientific, Waltham, MA, USA) was performed on cell/scaffold constructs on days 1 and 5 after seeding to visualize cellular morphology. Samples were preliminary fixed with paraformaldehyde (PFA) (Sigma-Aldrich, Schnelldorf, Germany) and incubated in 0.1% v/v Triton® X-100 (Merck, Darmstadt, Germany) diluted in PBS for 10 min at RT to permeabilize the cells and enhance antibody penetration. Samples were then rinsed three times with PBS (5 min per rinse) to remove any excess permeabilization agent. To block non-specific binding sites, samples were incubated in a blocking solution containing 1% Bovine Serum Albumin (BSA) (AppliChem GmbH, Darmstadt, Germany) and 22.52 mg ml^{-1} glycine (AppliChem GmbH, Darmstadt, Germany) in PBST 0.1% v/v Tween® 20 (Sigma-Aldrich, Schnelldorf, Germany) diluted in PBS for at least 30 min at RT. Following blocking, samples were incubated with the monoclonal antibody against TRITC-conjugated phalloidin (Sigma-Aldrich, Schnelldorf, Germany) diluted in 1% BSA in PBST at a concentration of 1 : 50. Given that the primary antibody is FITC-conjugated, and to ensure specific binding to the target proteins, the incubation took place in a dark humidified chamber overnight at 4 °C. Samples were then washed three times with PBS (5 min per wash) to remove any unbound antibody. To stain the cell nuclei, samples were incubated with a 1 : 1000 solution of 20 mg ml^{-1} DAPI diluted in PBS in a dark humidified chamber for 5 min at RT. Samples were then rinsed with PBS for 5 min and kept in PBS for subsequent imaging. The same procedure was followed for the visualization of cell adhesion using FITC-conjugated vinculin (495 nm excitation/519 nm emission) (Sigma-Aldrich, Schnelldorf, Germany) and cell nuclei using DAPI. The samples were imaged using a LeicaTCS-SP8 inverted confocal microscope (Leica, Wetzlar, Germany), allowing for the visualization and analysis of the immunofluorescent staining patterns.

2.4. Osteogenic response of MC3T3-E1 pre-osteoblastic cells under mechanical stimulation

2.4.1. Cell seeding of scaffolds prior mechanical stimulation. For the osteogenic experiments, a higher number of cells was initially seeded compared to the viability assays. In the viability assays, time points up to day 7 were used to monitor cell proliferation over time. For the osteogenic experiments, the scaffolds were seeded with a larger cell number, and after 24 h of incubation to allow initial cell attachment, the media was replaced with osteogenic medium and mechanical stimulation was applied. This procedure ensured that cells were properly adhered to the scaffolds before the dynamic

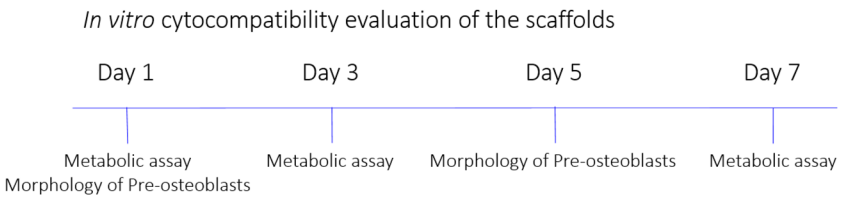

Fig. 2 Schematic timeline of the experiments.

stimulation began. More specifically, prior to seeding, all lyophilized scaffolds underwent sterilization through a 30 min exposure to UV radiation at a wavelength of 265 nm. Subsequently, the cells were seeded onto sterilized scaffolds at a density of 4×10^4 cells per scaffold and allowed to incubate for 1 h before additional culture medium was added, to facilitate the cell seeding process. After the initial cell attachment period, the medium was replaced with osteogenic medium, consisting of alpha-MEM™ supplemented with 10 nM dexamethasone (Sigma-Aldrich, Schnelldorf, Germany), 10 mM β-glycerophosphate (Sigma-Aldrich, Schnelldorf, Germany), and 50 μg ml^{-1} L-ascorbic acid 2-phosphate (Sigma-Aldrich, Schnelldorf, Germany). The cell-loaded scaffolds were cultured in this osteogenic medium for a specific duration and proper conditions to induce osteogenic differentiation. A timeline of the osteogenic experiments, for better visual understanding, and a more complete description of the experimental steps taken and timepoints chosen, is depicted in Fig. 3.

2.4.2. Mechanical stimulation protocol. The experiment was performed according to a procedure described in a recently published report of our research group.[31] Briefly, each cell-loaded scaffold was subjected to mechanical force using a MechanoCulture TX bioreactor equipped with uniaxial cyclic compression (CellScale, Waterloo, Canada). Prior to that, the scaffolds were sized appropriately in order to have a uniform shape for the mechanical tests and for further analysis. The diameter of each scaffold was 6 mm and the height was 6.5 mm after adjusting the size. For the mechanical stimulation experiments (Fig. 4), the cell-seeded scaffolds were rotated by 90°, as this is the direction of the elongated dimension (perpendicular) of the spread cells, in order for the cells to experience the mechanical forces along their cytosol and their protrusions. This setup ensures that the cells throughout the entire scaffold surface experience uniform compressive forces, better mimicking the multidirectional mechanical environment of bone tissue *in vivo*, as previously reported.[31,32] The compression was applied at a frequency of 1 Hz and with a strain equivalent to 10% of the scaffold side (resulting in a displacement of 0.5 mm). The frequency of 1 Hz was selected for the mechanical stimulation based on previous studies from

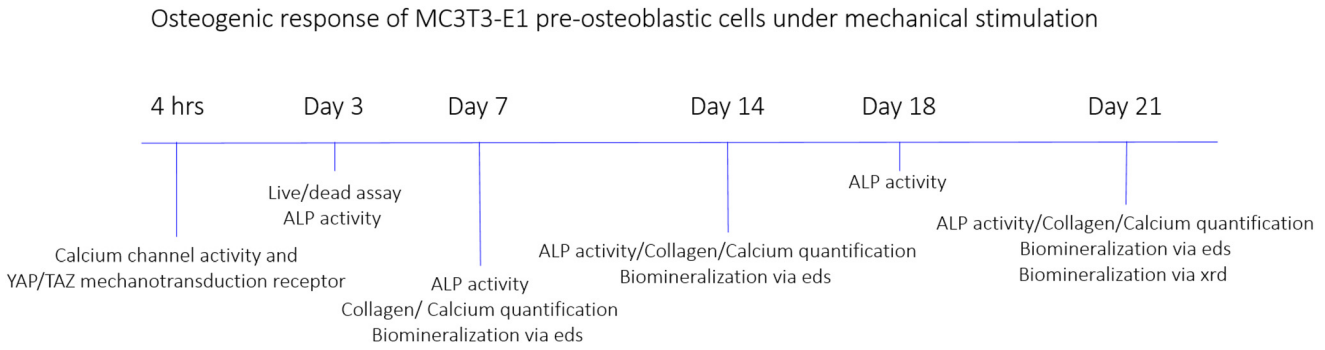

Fig. 3 Schematic timeline of the experiments.

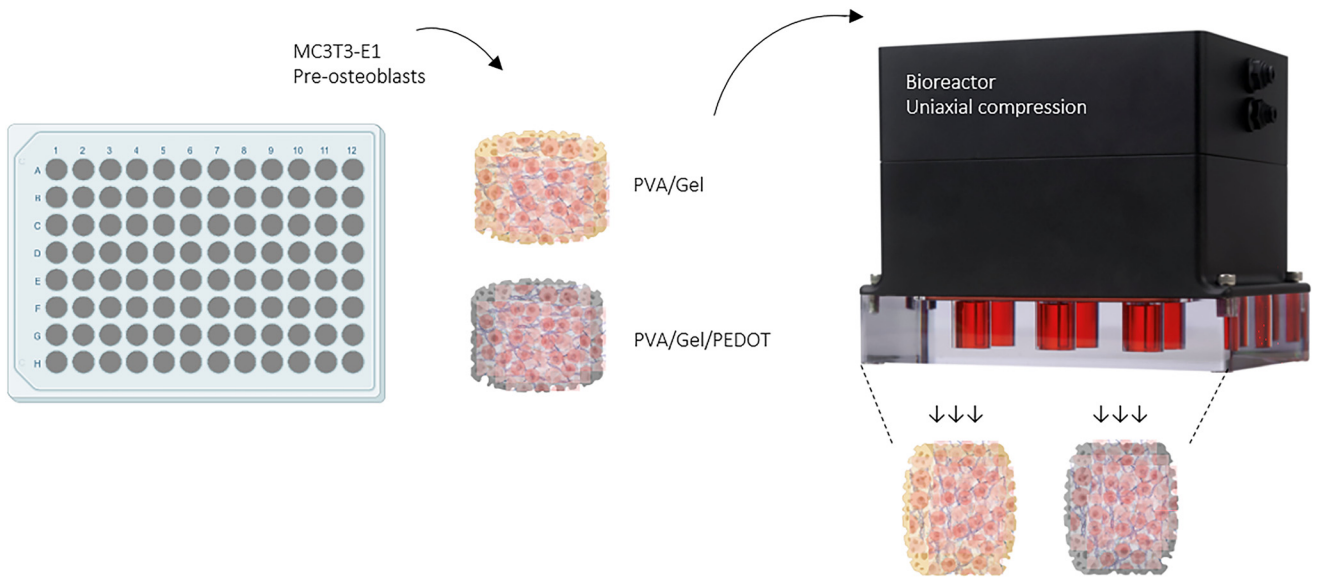

Fig. 4 Schematic view of the experimental set up for the mechanical stimulation of cell-loaded scaffolds (created with BioRender).

our group. Specifically, in ref. 31, we compared three different frequencies and demonstrated that 1 Hz produced optimal effects on cell behavior without compromising cell viability. Furthermore, in ref. 32, we successfully applied 1 Hz mechanical stimulation to cell-seeded scaffolds with two different cell types, recapitulating the bone environment, further validating this frequency as the most effective for promoting cell differentiation while maintaining viability. Each compression cycle lasted for 1 h and was performed daily, for a total duration of 21 days. The application of mechanical stress started the day after the addition of the osteogenic media, which was referred to as day 1 of the experiment. In order to compare the effects of dynamic (D) and static (S) conditions and further investigate the influence of mechanical stimulation on cell viability and differentiation, control static cultures were maintained under the same culture conditions without any mechanical stimulation.

2.4.3. In vitro cytocompatibility evaluation of mechanically stimulated constructs. The Live/Dead assay (Thermo Fisher Scientific) was employed to evaluate the viability of MC3T3-E1 pre-osteoblasts subjected to mechanical stimulation for 3 days. This assay aimed to determine whether mechanical loading exerted any adverse effects on cell viability. Briefly, the cell-loaded constructs were washed with PBS and stained with 4 μL of 2 μM calcein AM and 8 μL of 4 μM ethidium homodimer-1 (EthD-1) in 4 mL of PBS, and incubated in the dark for 1 h. Following incubation, the constructs were rinsed with PBS and imaged using a confocal laser fluorescence microscope (LeicaTCS-SP8, Wetzlar, Germany). Live cells exhibited green fluorescence (calcein AM), while dead cells were visualized in red (EthD-1), using appropriate filter settings. To quantify cell density at various time points, confocal images were analyzed using ImageJ software (version 1.54).

2.4.4. Calcium ion channel activity after mechanical stimulation. Intracellular free calcium on the pre-osteoblastic cells was determined using the Fluo-4 direct calcium assay kit (488 nm excitation/506 nm emission) (ThermoFisher Scientific, Waltham, MA, USA) according to the manufacturer's protocol. The aim of the assay was to observe the impact of mechanical stimulation and scaffold composition on the activation of calcium ion channels. Briefly, cell-loaded scaffolds were subjected to the same mechanical stimulation protocol that was previously described, but for a duration of 4 h. Before imaging, the scaffolds were incubated with the Fluo-4 AM reagent for 30 min and then rinsed with PBS. Observation of samples was carried out using confocal laser scanning microscopy (LeicaTCS-SP8, Wetzlar, Germany). Confocal images were acquired to visualize the activity of calcium ion channels of cells seeded onto the various scaffold compositions. The intensity was quantified by means of the Leica LASX software (version 3.7.6.25997).

2.4.5. Immunofluorescent staining of YAP/TAZ. Immunofluorescent staining of YAP/TAZ was performed on cell-seeded scaffolds that were mechanically stimulated for 4 h to investigate the presence and distribution of YAP/TAZ proteins, which are associated with the mechanotransduction pathways of cells. Paraformaldehyde (PFA)-fixed samples were incubated in 0.1% v/v Triton® X-100 (Merck, Darmstadt, Germany) diluted in PBS for 10 min at RT, to permeabilize cells and enhance antibody penetration. Samples were then thoroughly rinsed with PBS for 5 min to remove any excess permeabilization agent. To block non-specific binding sites, samples were incubated in a blocking solution containing 1% and 22.5 mg ml^{-1} glycine BSA (AppliChem GmbH, Darmstadt, Germany) in PBST with 0.1% v/v Tween® 20 (Sigma-Aldrich, Schnelldorf, Germany) diluted in PBS, for at least 30 min at RT. Following blocking, samples were incubated with the primary antibody against YAP/TAZ (Cell Signaling, Danvers, MA, USA) diluted in 1% BSA in PBST at a concentration of 1 : 200. The incubation took place in a humidified chamber overnight at 4 °C to ensure specific binding to the target proteins. Samples were then washed three times with PBS for 5 min per wash to remove any unbound primary antibody, followed by incubation with the secondary antibody (Anti-Rabbit Alexa Fluor 488) diluted in 1% BSA at a concentration of 1 : 1000, for 1 h at RT in the dark. To remove any unbound secondary antibody, samples underwent another series of three washes in PBS, each for 5 min. To stain the cell nuclei, samples were incubated in DAPI solution (1 : 1000 dilution of 20 mg ml^{-1} DAPI in PBS) for 5 min at RT, and rinsed with PBS for 5 min. The samples were examined using a Leica TCS-SP8 inverted confocal microscope (Leica, Wetzlar Germany). This imaging system allowed for the visualization of the immunofluorescent staining patterns. The distribution of YAP/TAZ was quantified by calculating the ratio of nuclear to cytosolic YAP/TAZ staining. This analysis was performed using ImageJ software (version 1.54), where a consistent threshold was applied across all images to ensure comparability. Particles corresponding to the nuclear and cytosolic portions of the staining were measured.

2.4.6. Detection of alkaline phosphatase (ALP) enzymatic activity. Alkaline phosphatase (ALP) is an enzyme that is widely distributed in different tissues and is particularly associated with bone formation, where it is involved in mineralization processes. The main role of this enzyme is to detach phosphate groups and consequently inducing the formation of HA crystals, which is a fundamental component of the extracellular matrix of bone tissue.[33] To assess the osteogenic differentiation of cells, ALP enzymatic activity was visualized using a live staining method. At predetermined time points, the cell-loaded scaffolds were subjected to ALP staining. The staining procedure detects the active enzyme by utilizing a substrate cleaved by ALP, resulting in a fluorescent signal (395 nm excitation/509 nm emission). The scaffolds were thoroughly washed with PBS and incubated with ALP live stain solution (Thermo Fisher Alkaline Phosphatase Live Stain, Thermo Fisher Scientific, Waltham, MA, USA) for 1 h at 37 °C. After staining, the scaffolds were rinsed with PBS and imaged by confocal laser scanning microscopy (LeicaTCS-SP8, Wetzlar, Germany). Images were acquired on days 3, 7, and 18 to visualize the distribution and intensity of ALP staining within the cell layer on the various scaffold compositions and conditions.

2.4.7. Biochemical determination of alkaline phosphatase (ALP) enzymatic activity. To assess the osteogenic differentiation of mechanically stimulated MC3T3-E1 cells, alkaline phosphatase (ALP) activity was measured at days 7, 14, and 21. The procedure followed a previously established protocol.[34] Briefly, scaffolds were rinsed twice with PBS for 20 minutes and subsequently incubated in 250 μL of lysis buffer containing 0.1% Triton X-100 and 50 mM Tris–HCl (pH 10.5). Samples underwent two freeze–thaw cycles, alternating between −20 °C and room temperature on a shaker (200 rpm) for 10 minutes each, to ensure complete cell lysis. Then, 10 μL of the lysate was combined with 100 μL of a 2 mg mL^{-1} *p*-nitrophenyl phosphate (pNPP) solution prepared in 50 mM Tris–HCl and 2 mM $MgCl_2$. After 1 hour of incubation at 37 °C, absorbance was recorded at 405 nm using a microplate reader (Synergy HTX, BioTek, USA). ALP activity was expressed in units of nmol *p*-nitrophenol produced per minute and normalized to total protein content, quantified *via* the Bradford assay (AppliChem GmbH, Darmstadt, Germany). Each condition was tested in quadruplicate ($n = 4$).

2.4.8. Collagen secretion measurements. The quantification of collagen secretion in the culture supernatants was performed using a protocol of our research group that is based on the Sirius Red staining method.[35] The Sirius Red staining method relies on the elongated, anionic structure of the dye molecule binding parallel to cationic collagen fibers.[36] Since gelatin originates from denatured collagen, it could interfere with Sirius Red–based collagen quantification. Gelatin is chemically crosslinked in the developed scaffolds and remains insoluble under culture conditions, making it unlikely to leach into the supernatant. Briefly, after 7, 14 and 21 days in culture, 25 μl of culture medium were diluted in 75 μl of ultrapure deionized water, mixed with 1 ml 0.1% w/v Sirius Red (Sigma-Aldrich, Schnelldorf, Germany) dye in 0.5 M acetic acid and finally incubated for 30 min at RT. The samples were then centrifuged at 15000*g* for 20 min at 4 °C, and washed with 0.5 M acetic acid to remove the non-bound dye. Finally, 1 ml of a 0.5 M NaOH solution was added to extract the collagen bound dye complex and measured in a spectrophotometer (Synergy HTX Multi-Mode Microplate Reader, BioTek, Winooski, USA). 200 μl of each solution were transferred to a 96-well plate and the measurements were taken at 530 nm. The absorbance values were correlated to the concentration of collagen by using a calibration curve. All samples were analyzed in quadruplicates ($n = 4$).

2.4.9. Calcium secretion measurements. Calcium secretion of the cell seeded scaffolds was determined by the O-cresol phthalein complexone (CPC) method (BIOLABO, Les Hautes Rives, France). In alkaline solution, CPC reacts with calcium to form a dark-red colored complex. The absorbance measured values are proportional to the amount of calcium in the specimen. Briefly, supernatants were collected, and 10 μl from each of them were mixed with 100 μl of calcium buffer and 100 μl of calcium dye containing 78 μmol l^{-1} CPC. Absorbance of the mixture was measured using a spectrophotometer (Synergy HTX Multi-Mode Microplate Reader, BioTek, Winooski, USA) at 550 nm. Absorbance values were correlated to calcium concentration by using a calibration curve. All samples were analyzed in quadruplicates ($n = 4$).

2.4.10. Energy dispersive spectroscopy (EDS) analysis. The EDS detector, integrated within the used scanning electron microscope (SEM) (JEOL JSM-6390 LV, MA, USA) collects the X-ray spectra emitted by the samples upon interaction with the SEM electron beam. The acquired spectra were analyzed to identify the presence and relative abundance of calcium and phosphorus, enabling quantitative and visualized assessment of biomineralization. The SEM images allowed the observation of the spatial distribution of calcium and phosphorus biomineralization onto the scaffold surface. The EDS analysis provided quantitative information on the elemental composition, allowing the determination of calcium and phosphorus ratios in the biomineralized regions.

2.4.11. X-ray diffraction (XRD) analysis. XRD was employed to explore the potential formation of apatite-like structures onto the scaffolds. To perform this analysis, the scaffolds were first freeze-dried for 24 h for water removal, to avoid excess background noise on the final spectrum. XRD analysis was performed by a triple axis in a high-resolution X-ray diffractometer (Bruker D8 Advance, Karlsruhe, Germany) with Cu Kα radiation ($\lambda = 1.5460$ Å), operating at 45 kV and 40 mA, for an angle step of 0.0241° and 2θ range from 20 to 60°. The obtained XRD patterns were analyzed to determine the composition of hydroxyapatite (HA) in the scaffold. The diffraction peaks were compared with those of calcium phosphate derivates and HA. The accuracy and reliability of the XRD analysis were ensured by performing triplicates of the measurements ($n = 3$).

2.5. *In vivo* experimentation

2.5.1. *In vivo* evaluation of subcutaneously implanted scaffolds in mice. Four three-month-old C57BL/6 mice were utilized in the experimental procedures. Laboratory animals were housed in the animal facility at IMBB-FORTH (EL91-BIOexp-02), according to Greek and European Legislations. All experiments were performed according to the Guide for Care and Use of Laboratory Animals and were approved by the Department of Welfare, Ministry of Agriculture, Greece (Laboratory Animal Protocol #69248, Primary Investigator Prof. Marina Vidaki). The mice were removed from the colony and allowed to acclimate to the designated room for two weeks before the scheduled surgery. This acclimation period ensured that the mice were accustomed to the environmental conditions in which they would be kept after the surgical procedures. Anesthesia was induced using isoflurane in a controlled and properly-ventilated induction chamber. Oxygen was supplied at a rate of 1–2 l min^{-1} to maintain the mice's respiratory function. Each mouse was introduced to the induction chamber, and isoflurane concentration (IsoVet 1000 mg g^{-1}) was gradually increased until the animal was fully anesthetized. Anesthesia was confirmed by the absence of the toe pinch reflex. The anesthetized mice were then transferred to a nose cone connected to the anesthesia machine and main-

tained at 2.5% isoflurane concentration throughout the surgery. To prevent hypothermia, the mice were placed on a warm heat-pad. After the surgical procedures, the mice were placed in clean recovery cages with access to fresh food and water through the cage lids. For analgesia, each mouse received a 60 µl intraperitoneal injection of 5 mg ml^{-1} meloxicam every 24 h for the following three days to manage post-operative pain and discomfort. After two weeks, the mice were euthanized, and their tissues were obtained for further processing. Euthanasia was performed by cervical dislocation. Depilatory cream was applied to the skin areas of interest, and the areas were washed with PBS. The skins, along with the attached implants, were isolated and washed with cold PBS. The tissues were then incubated in a 4% w/v PFA solution at 4 °C overnight. Cryosections of the tissues were obtained, followed by histochemical staining. Subsequently, cryoprotection was performed by immersing the samples in a 30% w/v sucrose solution for 12 h. The sucrose-fixed samples were then embedded in a solution composed of 7.5% w/v gelatin and 15% w/v sucrose, followed by snap-freezing in liquid nitrogen to facilitate sectioning. A cryomicrotome (Leica, Wetzlar, Germany) was used to cut sections with a thickness ranging from 15 to 20 µm.

2.5.2. Hematoxylin & eosin (H&E) staining. Tissue slices were hydrated with deionized water, immersed in hematoxylin for 45 s, and washed with deionized water. Slides were washed with PBS and were immersed in bluing solution for 1 min. Slides were then placed in 70% and 95% ethanol. Tissue slices were subsequently immersed in eosin solution for 45 s and then rinsed twice with 95% and 100% ethanol. Slides were finally placed in xylene for 1 min and were left to air-dry for 5 min. Entellan™ was used as the mounting medium. Slides were allowed to dry completely and were stored at RT. Images from H&E-stained tissue slides were obtained using a Zeiss Axioscop2 (Oberkochen, Germany) brightfield microscope with ProgRes CapturePro software (version 2.8.0).

For the staining of the cell nuclei and the actin cytoskeleton, slides with cryosections were placed in a humidity chamber to thaw for 20 min at RT. Thawed tissue slices were hydrated with PBS for 15 min and fixed with 4% w/v PFA (Sigma-Aldrich, Schnelldorf, Germany) for 10 min at RT. Tissue slices were gently rinsed with PBS for 5 min to remove excess fixative. Slices were then incubated in 0.3% v/v PBS-Triton, Triton® X-100 (Merck, Darmstadt, Germany) at RT, and rinsed with PBS. Tissue slices were incubated in blocking solution 5% v/v FBS (ThermoFisher Scientific, Waltham, MA, USA), 3% w/v BSA (AppliChem GmbH, Darmstadt, Germany) diluted in 0.1% v/v PBS-Triton for at least 1 h at RT. Actin filaments were stained with the actin marker phalloidin Alexa Fluor 488 (495 nm excitation/518 nm emission) (ThermoFisher Scientific, Waltham, MA, USA) for 20 min at 4 °C. Slices were then rinsed with 0.1% v/v PBS-Tween® 20 (Sigma-Aldrich, Schnelldorf, Germany) and PBS. To stain the cell nuclei, slices were incubated in a DAPI solution for 5 min at RT and rinsed with PBS. MOWIOL was used as slide mounting medium. The exact composition was 25% v/v glycerol anhydrous pure, 65% v/v deionized water, 10% w/v MOWIOL 4–88 Reagent (Calbiochem, San Diego, CA, USA) and 100 mM Tris–Cl pH:8.5 (Applichem, Darmstadt, Germany). Slides were allowed to dry completely at RT protected from light, and were stored at 4 °C.

2.6. Statistical analysis

All graphs presented in this study were prepared using GraphPad Prism software (version 8) (San Diego, CA, USA). Statistical analysis was performed (i) for the Young's modulus, % swelling ratio S and % surface porosity using the t test in GraphPad Prism software (version 8) (San Diego, CA, USA), (ii) for the % mass loss D, cell viability, calcium and collagen secretion assessment using the two-way ANOVA Dunnett's multi-comparison test in GraphPad Prism software (version 8) (San Diego, CA, USA), and (iii) for the mean fluorescence intensity of Fluo-4 calcium influx, YAP/TAZ localization and ALP activity using the one-way ANOVA test in GraphPad Prism software (version 8) (San Diego, CA, USA). P-Values indicate statistically significant differences, with (*) $p < 0.05$, (**) $p < 0.01$, (***) $p < 0.001$, (****) $p < 0.0001$, (*****) $p < 0.00001$.

3. Results

3.1. Physicochemical and mechanical characterization of scaffolds

The fabricated scaffolds' compositions as well as concentrations and crosslinking method are displayed in Table 1. All scaffolds were fabricated through lyophilization, and resemble sponge-like structures (Fig. 5A). Scaffolds containing PEDOT:PSS appear to be darker. Control PVA/gelatin scaffolds were white. Pores are detectable on all scaffolds macroscopically.

3.1.1. FTIR and Raman spectra analysis. FTIR spectra are a useful tool to identify the presence of certain functional groups in a molecule, as each specific chemical bond often has a unique energy absorption band. To better understand the bond formation and to detect the crosslinked structure and intermolecular interactions, we acquired the FTIR spectra of all scaffold types as well as their basic components in the range of 4000 cm^{-1} to 500 cm^{-1} wavenumbers. The results are presented in Fig. 5B. For pure gelatin we observed prominent bands corresponding to amide A, amide B, amide I, amide II and amide III regions.[37] The amide A band arises between

Table 1 Acronyms of the various scaffold compositions. PEDOT:PSS is the acronym for poly(3,4-ethylene dioxythiophene):poly(styrene sulfonate), PVA is the acronym for poly(vinyl alcohol), and GOPS is the acronym for (3-glycidyloxypropyl)trimethoxysilane

Scaffold acronyms	Composition
PVA/Gel	5% w/v PVA and 5% w/v gelatin, 0.025% w/v glutaraldehyde, serves as control
PVA/Gel/PEDOT	5% w/v PVA and 5% w/v gelatin, 0.15% w/v PEDOT:PSS, crosslinked with 2% v/v GOPS and 0.025% w/v glutaraldehyde

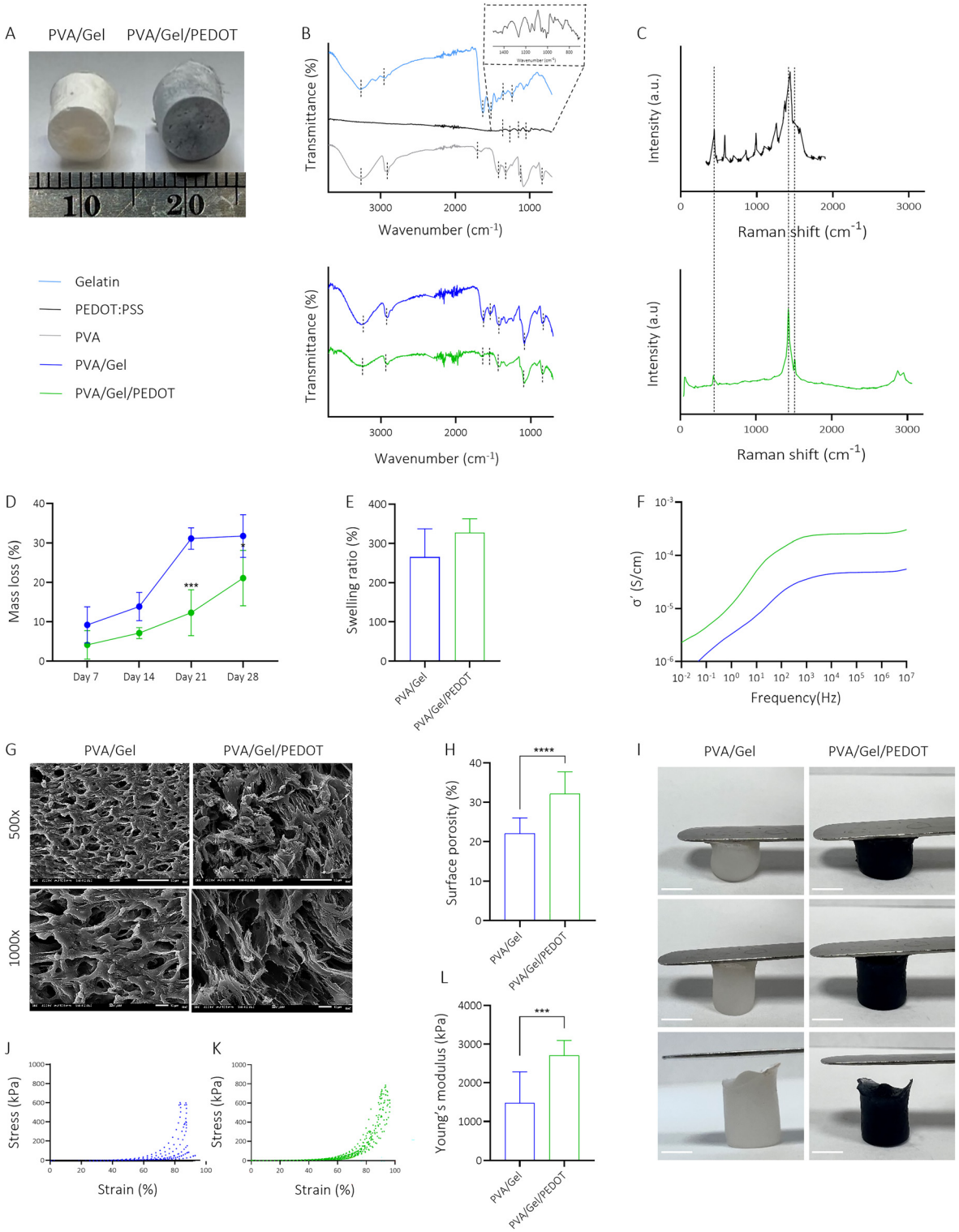

Fig. 5 (A) Macroscopic view of freeze-dried scaffolds. (B) FTIR spectra of the basic components, gelatin, PEDOT:PSS and PVA and the different scaffold types. (C) Raman spectra of the basic component PEDOT:PSS and the PVA/Gel/PEDOT scaffold. (D) The % mass loss after 28 days in culture. (E) Swelling ratios of the lyophilized scaffolds after 3 h of immersion in PBS. (F) Evaluation of the scaffold electrical conductivity. (G) Surface porosity of both scaffold compositions depicted *via* SEM in two magnifications (500× upper panel, and 1000× lower panel; scale bars represent 50 μm and 10 μm respectively). (H) Evaluation of % surface porosity calculated *via* SEM images using ImageJ. (I) Macroscopic view of scaffolds when hydrated and manually compressed using a spatula. After compression, they fully recovered retaining their initial shape (scale bar represents 4 mm). Stress–strain curves after uniaxial compression using mechanical testing of (J) PVA/Gel and (K) PVA/Gel/PEDOT scaffolds. (L) Evaluation of elastic modulus of the scaffolds at 60–90% strain, at a velocity of 15 mm s^{-1}. Statistical analysis denotes a statistically significant difference compared to the corresponding PVA/Gel control scaffold (*p < 0.1, ***p < 0.001, ****p < 0.0001). Lack of asterisks indicate non-significant differences. All values are presented as mean ± standard deviation.

3200–3500 cm^{-1} where the stretching vibrations of N–H bonds can be found. At the same region O–H bonds are present. Also, a peak around 3100 cm^{-1} is related to the asymmetric stretching of C–H bonds, associated with amide B. Moreover, there is an intense peak at 1600–1700 cm^{-1} which indicates the presence of C═O bonds, attributed to amide I. The amide II band typically observed at 1500–1600 cm^{-1} shows a peak attributed to the combination of N–H bending and C–N stretching vibrations. Finally, regarding the amide III, a peak at 1200–1300 cm^{-1} corresponds to the deformation of N–H bonds and the bending of C–N bonds.[38] Pure PVA exhibits a broad peak between 3200–3500 cm^{-1}, indicating the stretching vibrations of –OH hydroxyl groups. Nearby a peak at 2850–3000 cm^{-1} due to C–H stretching, can be found. The carbonyl group C═O stretching vibrations occur around at 1750 cm^{-1}. Furthermore, peaks at 1450 cm^{-1} and 1350 cm^{-1} are associated with the C–H and O–H bending, respectively. In addition, a peak at 1100 cm^{-1} is observed attributed to the C–O deformation.[39,40] For pure PEDOT:PSS, C–C and C═C stretching of the aromatic rings of PSS are represented by the spikes at around 1650 cm^{-1}. Also, a peak at 1090 cm^{-1} represents the C–O–C stretching vibration band of PEDOT rings. Finally, mild peaks were seen at 1200 cm^{-1} and 960 cm^{-1} corresponding to the stretching vibration of SO_3H group of PSS and to the C–S bonds in the thiophene ring of PEDOT.[41,42] PEDOT:PSS-containing scaffolds have most of the characteristic peaks of pure PEDOT:PSS, validating the crosslinking between PVA/Gel matrix and PEDOT:PSS. In addition to the FTIR analysis, and considering that PEDOT:PSS characteristic peaks are not easily distinguishable in the infrared spectra due to their low intensity, Raman spectroscopy was performed on the pure PEDOT:PSS and the PVA/Gel/PEDOT scaffolds. Raman spectroscopy provided additional confirmation of PEDOT:PSS incorporation within the scaffold matrix. As reported in the literature,[43] PEDOT:PSS exhibits characteristic Raman bands at 1563 cm^{-1} and 1532 cm^{-1} (asymmetric C_α═C_β stretching), 1421 cm^{-1} (symmetric C_α═C_β (–O) stretching), 1368 cm^{-1} (C_β–C_β stretching), and 1256 cm^{-1} (C_α–C_α inter-ring stretching). Additional peaks are typically observed at 1093 cm^{-1} (C–O–C deformation), 989 cm^{-1} (oxyethylene ring deformation), 701 cm^{-1} (symmetric C–S–C deformation), 577 cm^{-1} (oxyethylene ring deformation), and 437 cm^{-1} (SO_2 bending). The most characteristic signals of PEDOT:PSS were also evident in the Raman spectrum of the PVA/Gel/PEDOT scaffold (Fig. 5C), confirming the successful incorporation of PEDOT:PSS into the polymeric network. As for the PVA/Gel control scaffolds, the peaks of their basic components are present, as identified by the FTIR analysis, verifying a well-established bonding between those groups and the different charged groups of gelatin (positive)[44] and PVA (negative).[45] The peak correlating with the formation of the C═C bond in PEDOT is visible at approximately 1600 cm^{-1}, indicating the successful attachment of GOPS to the interpenetrating polymer network of PEDOT:PSS.[46] As for the possible crosslinking reaction mechanism between PEDOT:PSS and GOPS, it is reported in the literature that the SO_3^- groups of the excess PSS react with the epoxy ring of GOPS.[47] In the case of gelatin, glutaraldehyde reacts with each functional amino group of adjacent lysine residues, while in PVA, glutaraldehyde reacts with two adjacent hydroxyl groups, forming acetal bridges.[48]

3.1.2. Degradation and dissolution analysis. Degradation/dissolution rates for the various scaffold compositions after 7, 14, 21, and 28 days are demonstrated in Fig. 5D. PVA/Gel control scaffolds indicated the highest degradation/dissolution rates. This could be attributed to the low concentration of the crosslinking agent (glutaraldehyde), leading to incomplete crosslinking, and the time frame during which the crosslinking reaction occurred. Conversely, the dual crosslinked PVA/Gel/PEDOT scaffolds had lower values than the corresponding control PVA/Gel, at all time points. In general, PEDOT:PSS-containing scaffolds maintained their initial weight and integrity for longer periods of time in culture conditions.

3.1.3. Swelling ratios. The freeze-dried scaffolds were allowed to absorb the maximum volume of PBS for 24 h. PEDOT:PSS-containing scaffolds possessed the ability to swell. Liquid uptake is exhibited in Fig. 5E. PVA/Gel/PEDOT exhibit higher values (327 ± 29%) compared to the control (266 ± 58%).

3.1.4. Electrical conductivity of scaffolds. We have performed conductivity measurements on hydrated scaffolds by Broadband Dielectric Spectroscopy (BDS). Results of frequency dependent conductivity (real part σ') derived from BDS measurements are shown in Fig. 5F.

By fitting σ' data by the function:

$$\sigma' = \frac{\sigma_0}{(2\pi f)^{m-1}}$$

that expresses the frequency dependence of conductivity in disordered systems,[49] the values of static conductivity σ_0 and the respective exponent m for our scaffolds have been derived. Data analysis shows the presence of two different regimes of conductivity (*i.e.*, m exponents) in the low frequency (10^{-2}–1 Hz) and high frequency (10^2–10^7 Hz) ranges, that can be ascribed to different mechanisms of conduction.[49] Fitting results for both static conductivity σ_0 and m exponent are reported in Table 2. Usual ohmic conduction corresponds to an exponent $m = 1$.

3.1.5. Porosity of scaffolds. Porosity of all scaffolds was visualized through SEM images (Fig. 5G) at two magnifications (500× first panel, and 1000× second panel). Moreover, quantification of the SEM images using ImageJ (version 1.54), is shown in Fig. 5H. PVA/Gel/PEDOT scaffolds demonstrated significantly higher surface porosity levels (32 ± 6%) compared to

Table 2 Conductivity fitting results for the analyzed samples

% PEDOT:PSS	Low frequency, σ_0 [S cm^{-1}]	Low frequency, m exponent	High frequency, σ_0 [S cm^{-1}]	High frequency, m exponent
0.0	1.62×10^{-6}	0.61	0.023×10^{-3}	0.95
0.15	5.89×10^{-6}	0.61	0.166×10^{-3}	0.97

the control scaffolds. PVA/Gel control scaffolds proved to have fewer pores and a denser structure with a surface porosity of 22 ± 4%.

3.1.6. Mechanical properties. The scaffolds were measured when hydrated in order to provide an approximation of the pressure that the materials can withstand in a liquid environment such as the human body. No major morphological changes were observed after compression. A macroscopic view of hydrated manually compressed scaffolds is exhibited in Fig. 5I. The stress–strain curves obtained from the compression test of the PVA/Gel and PVA/Gel/PEDOT scaffolds are presented in Fig. 5J and K. Fig. 5J corresponds to PVA/Gel scaffolds and Fig. 5K to PVA/Gel/PEDOT scaffolds. The quantification of the Young modulus is presented in Fig. 5L. The mechanical tests indicated that the Young modulus of PVA/Gel/PEDOT scaffolds was 2.7 ± 0.4 MPa, which was significantly higher compared to the PVA/Gel control scaffolds with values at 1.5 ± 0.8 MPa.

3.2. *In vitro* cytocompatibility evaluation of the scaffolds

3.2.1. Imaging of pre-osteoblastic cells within the scaffolds. Confocal laser microscopy was employed to investigate the cell morphology and adhesion characteristics. In Fig. 6A, cell morphology is depicted. On day 1, PVA/Gel appears to have more cells with regular morphology compared to the PEDOT-containing scaffolds. This suggests healthy cellular adhesion and proliferation at this early time point. In contrast, scaffolds incorporating PEDOT displayed a notable reduction in cell presence at day 1. However, by day 5 a shift occurs as all scaffolds showcased significant increase in cell proliferation. Notably, PVA/Gel/PEDOT exhibited the most pronounced increase in cell numbers, suggesting its enhanced cytocompatibility. The consistency of these observations with cell adhesion visualization (Fig. 6B) highlights the significance of PEDOT in shaping cellular behaviors within bioengineered environments.

3.2.2. Viability and proliferation of pre-osteoblastic cells within the scaffolds. The cell viability and proliferation of the pre-osteoblastic cells in the different hydrogels was quantitatively assessed after 1, 3, and 7 days in the culture, and data are shown in Fig. 6C. The experiment was performed one day after seeding to assess early cell attachment and survival. The observed differences in OD values on day 1, particularly the lower values on the PEDOT-containing scaffolds, may be attributed to an initial cellular adaptation phase. It is likely that cells interacting with the PEDOT-modified surfaces required more time to adjust to the altered physicochemical environment, temporarily affecting their metabolic activity and attachment efficiency. This effect appears to be transient, as cell viability significantly increases over the following days (Day 3 and Day 7), indicating that the cells successfully adapt and proliferate on the PEDOT-containing scaffolds over time.

3.3. Osteogenic response of MC3T3-E1 pre-osteoblastic cells

The acronyms of each composition and the experimental conditions for the osteogenic response evaluation are displayed in Table 3.

3.3.1. Evaluation of *in vitro* cytocompatibility of mechanical stimulated constructs. The *in vitro* biocompatibility of the mechanically stimulated scaffolds was evaluated by Live/Dead staining and the quantification of the images was conducted *via* ImageJ software (version 1.54) (Fig. 6D). From the confocal images, we observed high levels of cell proliferation under both static and dynamic conditions, evidenced by dense networks of calcein–positive (live) cells. However, the dynamically stimulated scaffolds exhibited a greater number of EthD-1-positive (dead) cells compared to the static control. The increase in dead cells could be attributed to the mechanical stimulation protocol that may have caused some adverse effect on cell viability due to the forces applied to the cell membrane. Another observation is that the PVA/Gel/PEDOT_D scaffold exhibited slightly increased cell death (12 ± 2%) compared to the other compositions/conditions. These findings correlate with the metabolic assay results, where PEDOT–containing scaffolds in static culture, at day 1 exhibited lower values and increased cell numbers by day 7. Overall, despite the slight increase in cell death under dynamic stimulation, both PVA/Gel_D (92 ± 2%) and PVA/Gel/PEDOT_D (88 ± 2%) exhibited high cell viability, confirming their suitability for mechanically active bone tissue applications.

3.3.2. Determination of the calcium ion (Ca^{2+}) channel activity. Pre-osteoblasts play critical roles in bone formation and sensory transduction following stimuli on the bone surface. Exogenous stimuli elicit bone sensitivity, resulting in cellular deformation. Piezo1 channels have been implicated in mechanosensitive processes, as well as Ca^{2+} signals in osteoblasts. To this scope, we examined functional expression of the Piezo1 channel by recording direct mechanical stimulation-induced Ca^{2+} signaling in MC3T3-E1 pre-osteoblasts seeded in the different scaffolds. This assay aimed to validate the effect of the mechanical stimulation and the presence of PEDOT:PSS in this process. Confocal laser microscopy observation of Ca^{2+} influx revealed that mechanical stimulation of both scaffolds provides an enhancement of intracellular free calcium concentration [Ca^{2+}] (Fig. 6E). Statistical analysis indicated significantly higher calcium ion influx in the PVA/Gel/PEDOT_D condition compared to the PVA/Gel_S condition. Additionally, although PVA/Gel_D present a significant upregulation, PVA/Gel/PEDOT appears to have the highest values in both conditions, with the dynamic one being the most prominent. The above statement suggests an enhanced calcium channel activity in response to conductivity provided by PEDOT:PSS under mechanical stimulation.

3.3.3. Evaluation of the mechanotransduction receptor activity. Subcellular localization of YAP and TAZ was determined by immunofluorescence, followed by quantitative analysis of nuclear *versus* cytosolic distribution. Confocal laser microscopy revealed distinct patterns of YAP/TAZ distributions within the cellular population seeded onto the scaffolds. Specifically, cells subjected to mechanical stimulation exhibited pronounced nuclear localization of YAP/TAZ, indicative of their activation in response to mechanical cues. As shown in Fig. 6F, in all mechanically stimulated scaffolds, YAP/TAZ

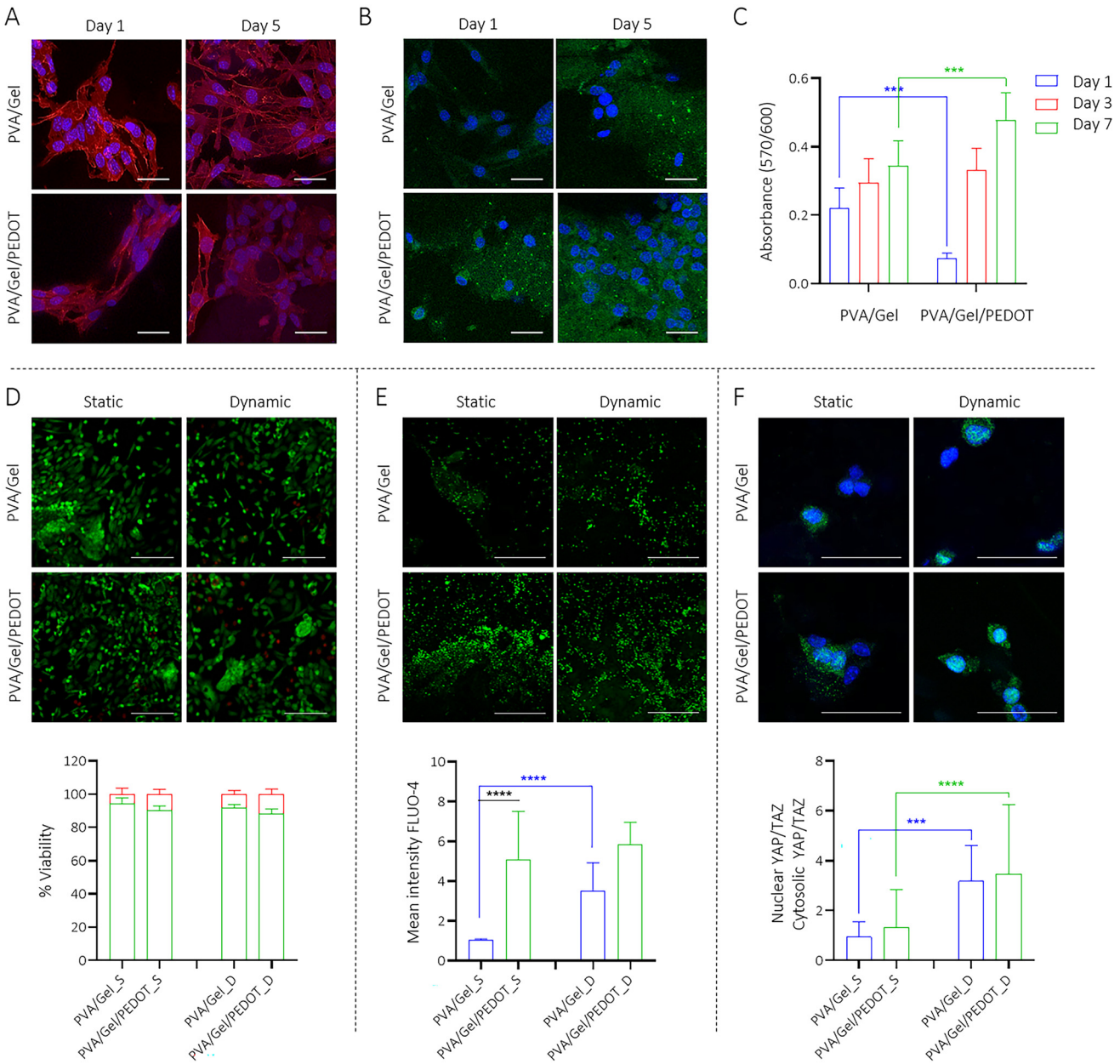

Fig. 6 Phalloidin (red) staining showing the (A) actin cytoskeleton of pre-osteoblasts, (B) vinculin staining (green) indicating focal adhesion points, cell nuclei were stained with DAPI (blue) (scale bar represents 50 μm). (C) Metabolic activity of cells on days 1, 3, and 7. (D) Live (green)/Dead (red) staining and quantification of % viability after 3 days of mechanical stimulation (scale bars represent 100 μm). Evaluation of mechanosensation after mechanical stimulation. (E) Fluo-4 staining (green) showing calcium ion channel activity, and fluorescence quantification (scale bars represent 500 μm). (F) YAP/TAZ mechanosensitive receptor staining (green) and quantification of the nuclear to cytosolic ratio of YAP/TAZ, nuclei counter-stained with DAPI (blue) (scale bars represent 50 μm). Significant differences when comparing the static *vs.* the dynamic culture are depicted in colored (blue and green) asterisks, while comparing PEDOT:PSS *vs.* control scaffolds are shown in black asterisks. 'S' designates static culture and 'D' dynamic culture (under mechanical stimulation) (***$p < 0.001$, ****$p < 0.0001$, denote a statistically significant difference compared to the corresponding control scaffold for each condition). Lack of asterisks indicate non-significant differences. All values are presented as mean ± standard deviation.

mainly localized in nuclei, while in statically cultured samples YAP/TAZ mainly localized in cytoplasm. This nuclear translocation of YAP/TAZ suggests their involvement in mechanotransduction pathways, where mechanical forces applied on the scaffold matrix trigger intracellular signaling cascades leading to changes in gene expression and cellular behavior. Quantification of the nuclear to cytosolic YAP/TAZ ratio confirmed this trend, with significantly higher nuclear localization under dynamic stimulation compared to the static culture, particularly when PEDOT is incorporated.

Table 3 Acronyms of the various scaffold compositions and the experimental conditions static (S) and dynamic (D). 'D' indicates the conditions performed using a mechanical stimulation protocol as described in section 2.4.2

Scaffold acronym	Experimental culture condition (static/dynamic)
PVA/Gel_S	PVA/Gel under static culture condition
PVA/Gel_D	PVA/Gel under dynamic culture condition
PVA/Gel/PEDOT_S	PVA/Gel/PEDOT under static culture condition
PVA/Gel/PEDOT_D	PVA/Gel/PEDOT under dynamic culture condition

3.3.4. Detection of ALP enzymatic activity. In Fig. 7A, green fluorescent signals represent the enzymatic activity of ALP as detected by live staining and visualized using confocal microscopy. The intensity and distribution of these signals were quantified by means of the Leica LASX software (version 3.7.6.25997) (Fig. 7B). The fluorescent regions primarily coincide with areas of cell presence, indicating active ALP within the cellular microenvironment. The PVA/Gel control scaffolds under mechanical stimulation present an upregulation of ALP expression eight-fold at day 7 and four-fold until day 18. The introduction of PEDOT led on upregulation in both static and dynamic conditions with the most significant one obtained upon stimulation. After 7 days in culture, significant differences with the control for both conditions were noted. Until day 18, a five-fold increase of ALP activity upon stimulation is evidenced. PVA/Gel/PEDOT presented the highest osteoconductive character, in terms of ALP activity, in both static and dynamic conditions. While it cannot be entirely ruled out that secreted soluble ALP adsorbed from the polymer surface contributes minimally to the signal, this is unlikely to represent a major source of fluorescence, due to the observed localized patterns and consistency with typical ALP activity patterns reported in the literature.[50]

3.3.5. Biochemical determination of alkaline phosphatase (ALP) enzymatic activity. Normalized ALP activity was evaluated at three different time points (day 7, 14 and 21) to assess the osteogenic response of pre-osteoblasts seeded on the

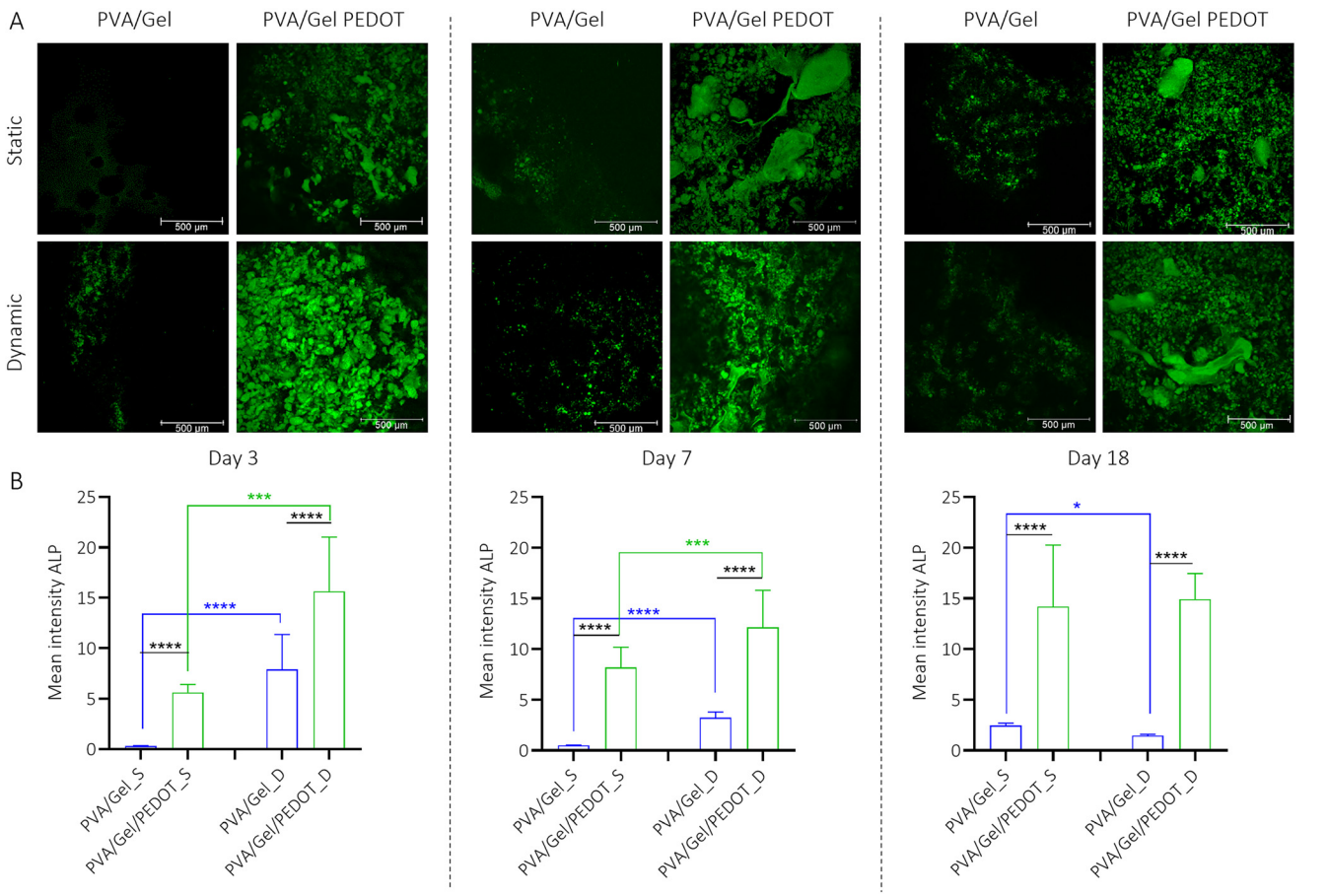

Fig. 7 (A) ALP enzymatic activity on days 3, 7 and 18 observed by confocal laser scanning microscopy following live staining (green). The scale bar represents 500 µm. (B) Quantification of fluorescence mean intensity from the confocal images. Significant differences when comparing the static *vs.* the dynamic culture are depicted in colored (blue and green) asterisks, while comparing PEDOT:PSS *vs.* control scaffolds are shown in black asterisks. 'S' designates static culture and 'D' dynamic culture (under mechanical stimulation) (*$p < 0.05$, ***$p < 0.001$, ****$p < 0.0001$, denote a statistically significant difference compared to the corresponding control scaffold for each condition). Lack of asterisks indicate non-significant differences. All values are presented as mean ± standard deviation.

scaffolds under static and dynamic culture conditions. As shown in Fig. 8A, under static conditions, no statistically significant differences were observed between the PVA/Gel and PVA/Gel/PEDOT scaffolds at any time point. However, when mechanical stimulation was applied, both scaffold types demonstrated an increase in ALP activity compared to their static counterparts, suggesting that dynamic culture promoted osteogenic differentiation. Notably, the PVA/Gel/PEDOT scaffold exhibited significantly higher ALP activity than its static equivalent across all time points, highlighting the synergistic effect of electroconductivity and mechanical stimulation on osteogenic activity. Moreover, these findings are consistent with the ALP immunofluorescence staining results (Fig. 7), where cells on dynamically stimulated PVA/Gel/PEDOT scaffolds displayed more intense ALP expression compared to those on statically cultured PVA/Gel scaffolds. The above results suggest that mechanical cues enhance osteogenic differentiation of pre-osteoblasts, with conductive environments further facilitating mechanotransduction and osteogenic signaling.

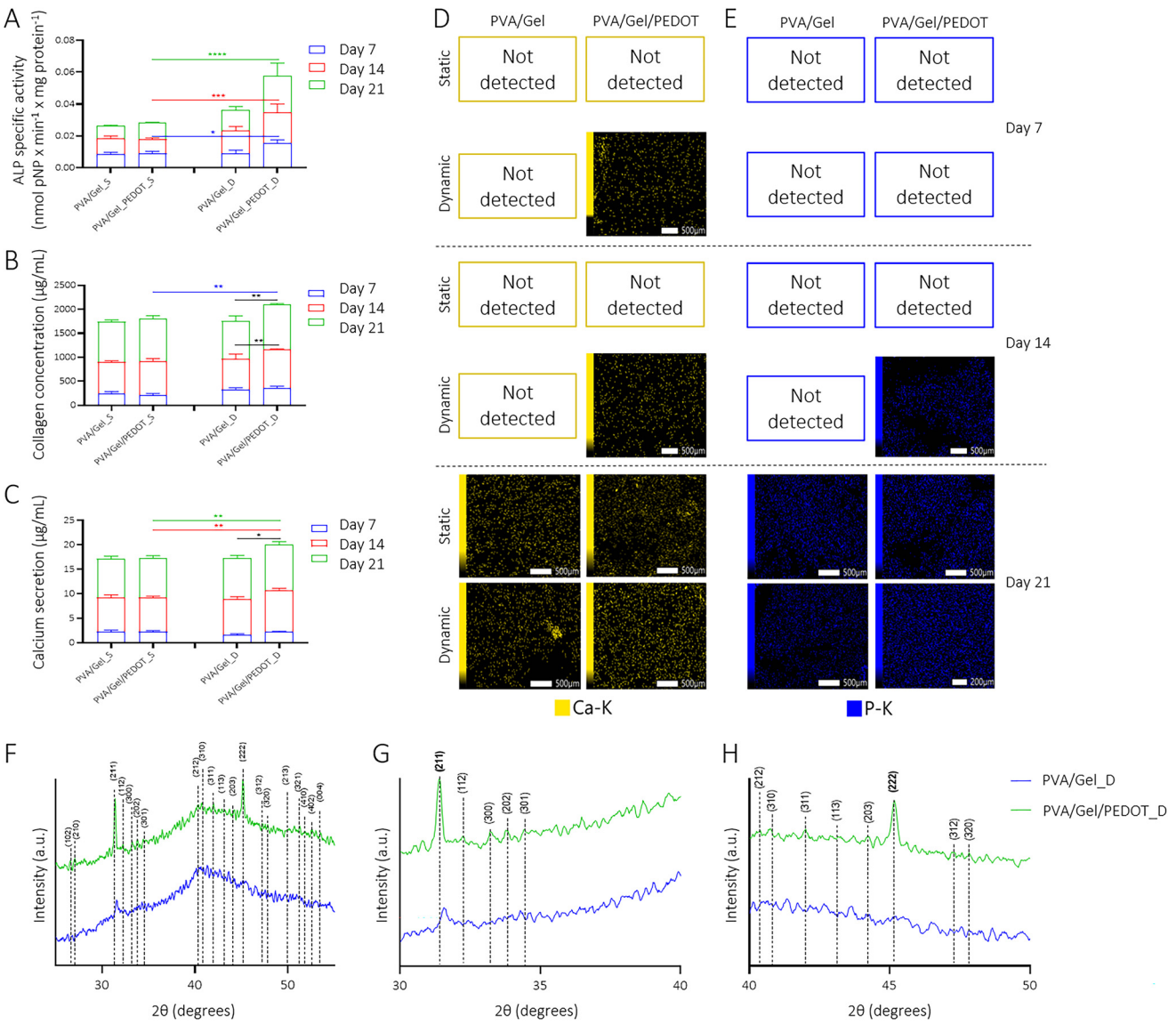

Fig. 8 Determination of (A) ALP activity, (B) collagen concentration and (C) calcium secretion levels on days 7, 14, and 21. Significant differences when comparing the static *vs.* the dynamic culture are depicted in colored (blue, green and red) asterisks, while comparing PEDOT:PSS *vs.* control scaffolds are shown in black asterisks (*$p < 0.05$, **$p < 0.01$, denote a statistically significant difference compared to the corresponding control scaffold for each condition). Lack of asterisks indicate non-significant differences. All values are presented as mean ± standard deviation. Determination of (D) the calcium and (E) phosphorus mineralization through elemental mapping by EDS analysis. Calcium is shown in yellow and phosphorus in blue. The scale bar represents 500 µm. (F) XRD analysis of mineralized scaffolds at day 21. Magnification of XRD spectra in the 2θ range of (G) 30°–40° and (H) in the 2θ range of 40°–50°. 'S' designates static culture, while 'D' dynamic culture (under mechanical stimulation). Dashed lines indicate the most characteristic peaks of natural bone HA.

3.3.6. Synthesized collagen quantification. The evaluation of collagen concentration (Fig. 8B) revealed a universal increase. The scaffolds provided production of comparable collagen levels under both dynamic and static culture conditions. Levels of collagen secreted by pre-osteoblasts on different scaffolds types demonstrated a three-fold increase from day 7 to day 14. On day 7, the levels of collagen concentration for PVA/Gel/PEDOT_D were significantly higher compared to the respective non-stimulated scaffolds. By day 21, all mechanically stimulated scaffolds indicated higher levels of collagen concentration compared to the static equivalents, with PVA/Gel/PEDOT_D retaining the highest values.

3.3.7. Calcium production measurement. Calcium levels for the different scaffolds are presented in Fig. 8C. The results indicate that there is a consistent and steady increase in calcium concentration over time in all scaffolds, implying continuous differentiation of pre-osteoblasts into mature osteoblasts until day 21. Notably, the scaffolds subjected to mechanical stimulation exhibited higher values, suggesting that mechanical stimulation enhances the differentiation potential. Particularly, PVA/Gel/PEDOT_D was the composition with significantly higher levels of calcium compared to their static equivalents on both day 14 and day 21.

3.3.8. EDS analysis of biomineralization. EDS analysis revealed the presence of calcium and phosphorus deposition for various scaffolds. Specifically, as shown in Fig. 8D, at day 7 only PVA/Gel/PEDOT_D demonstrated evidence of calcium deposition. At day 14, in dynamic culture PVA/Gel/PEDOT_D scaffolds exhibited calcium deposition. These results are in line with the previously examined osteogenic markers, highlighting the key role of PEDOT:PSS as a component that promotes osteogenesis. At day 21, calcium deposition is present onto all scaffolds. Regarding phosphorus, as shown in Fig. 8E, biomineralization is being observed in all scaffolds at day 21, in contrast with day 14 where phosphorus is presents only on PVA/Gel/PEDOT_D scaffolds. The identification of these elements is highly indicative of biomineralization, a fundamental process for the formation of mineralized tissues such as bone. The presence of calcium and phosphorus suggests the potential creation of HA, a major component of natural bone. In that respect, Ca/P ratios were evaluated *via* EDS analysis for both compositions. EDS analysis revealed that the PVA/Gel/PEDOT_D had very similar Ca/P ratio with HA (1.66) on day 21, as summarized in Table 4, suggesting the likelihood of biomineralization due to osteogenesis.

3.3.9. XRD analysis of biomineralization. The crystal structure of the mineral formed from the pre-osteoblastic cells onto the scaffold was determined by X-ray diffraction (Fig. 8F). From the initial graph, two zoomed plots were obtained, in the 2θ range of 30°–40° and 40°–50°, for a more detailed analysis of the peaks (Fig. 8G/H). The most characteristic peaks of HA,[51] which match with the 2θ positions of the peaks evident in the XRD plot of the two scaffolds, are shown as the dashed lines. The results of the XRD analysis reveals the presence of prominent peaks corresponding to potential formation of a biomineralized matrix. Specifically, PVA/Gel/PEDOT _D, the scaffold with the most promising EDS results, was removed from culture at day 21 and further investigated through XRD analysis, while PVA/Gel was included as control scaffold. PVA/Gel_D does not seem to have any sharp peaks, except a small one at a 2θ angle of approximately 32°. PVA/Gel/PEDOT _D appears to have sharp peaks at around 32° and 45°.[52] These peaks come from diffraction on (211) and (222) crystallographic planes of HA phase, respectively, and are used as reference markers for the identification of hydroxyapatite. Peaks with a lower intensity may be attributed to organic impurities of the scaffolds.[53] The comparison of the Ca/P ratio of PVA/Gel/PEDOT _D with the established Ca/P ratio of HA (1.67),[54] in combination with XRD analysis, significantly strengthen the evidence supporting the hypothesis of HA formation on the scaffold by mature osteoblasts. Overall, the examination underscores the scaffolds' capacity to support differentiation, highlighting their suitability for promoting bone tissue regeneration.

Table 4 Ca/P ratios of two different scaffold compositions on day 21, calculated following EDS analysis

Scaffold acronym	Ca/P ratio
PVA/Gel_D	1.20
PVA/Gel/PEDOT_D	1.66

3.4. *In vivo* evaluation of implanted scaffolds by histochemical analysis

All animals survived the implantation procedure without any clinical evidence of wound infection or inflammation. Histological H&E staining (Fig. 9) revealed the formation of a collagen-rich area surrounding the implanted scaffolds, a typical formation following a biomaterial implantation in immunocompetent hosts. After 14 days of treatment, the surrounding tissues of the implanted specimen showed no immune recruitment or macrophage fusion. Specific cell types involved were not characterized in this study. Further staining (Fig. 9C and D right) of cell nuclei and actin confirmed cell infiltration inside the implants, especially for PVA/Gel/PEDOT. Overall, no signs of foreign body reaction were observed as evaluated by the histological assessment of the implantation of both constructs in mice.

4. Discussion

Tissue engineering employs cells and biomaterials, aiming to engineer biocompatible platforms that support tissue formation. The development of biodegradable electroactive scaffolds is an intriguing area of research since natural bone possesses both endogenous conductive and electroactive properties.[55] To ensure successful bone tissue repair and regeneration, numerous physiological signals, such as biochemical, electrical, and mechanical signals, are required.[56] This study presents the design of electroconductive, mechanoactive

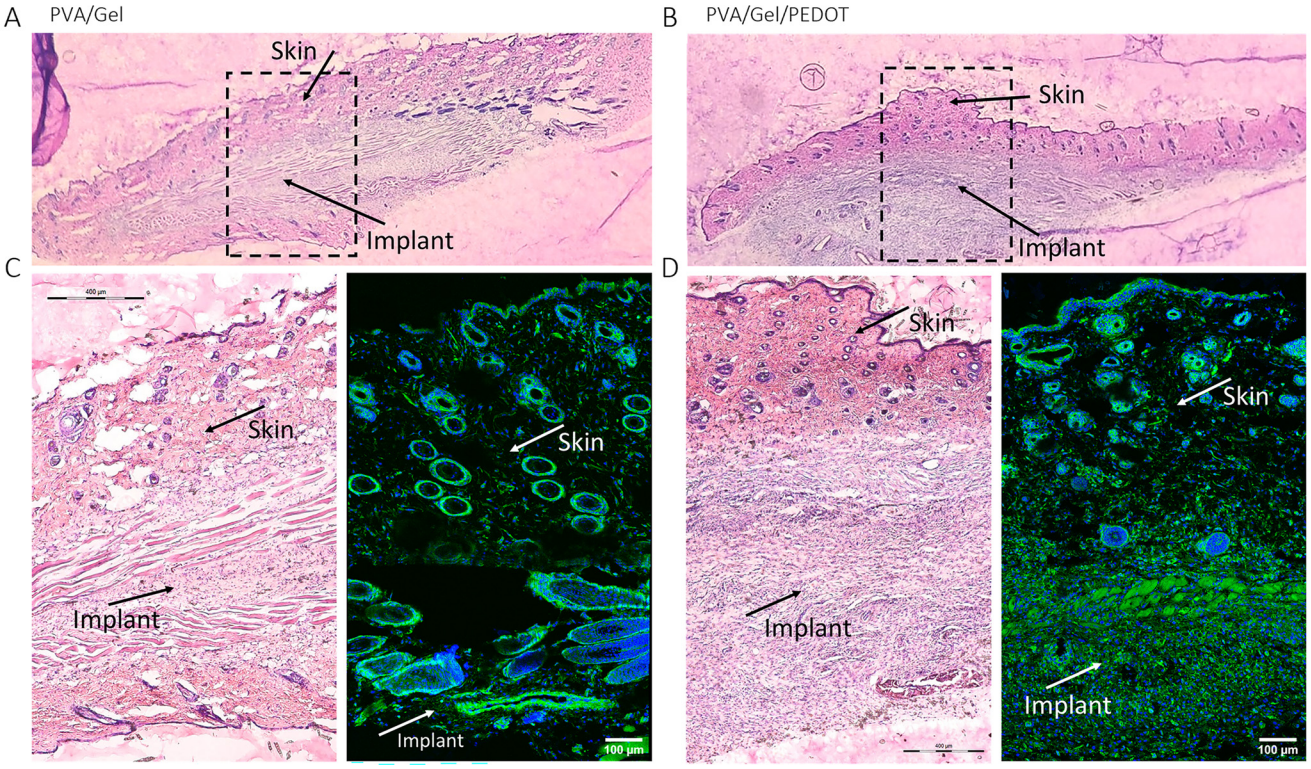

Fig. 9 Histological assessment of cryosections of explanted constructs after subcutaneous implantation of the control and PVA/Gel/PEDOT scaffolds. Hematoxylin & eosin stain of (A) PVA/Gel and (B) PVA/Gel/PEDOT. (C and D left) Magnification of the dashed rectangle of A and B images (scale bar represents 400 μm), and (C and D right) Cell nuclei (blue) and actin (green) stained sections of epidermal/subcutaneous tissue around the implanted scaffolds (scale bar represents 100 μm). The arrows indicate the position of the implants.

scaffolds incorporating PEDOT:PSS into a PVA/gelatin matrix and their validation for bone tissue engineering. These scaffolds were engineered to mimic the intrinsic mechanoelectrical properties of native bone, supporting the hypothesis that mechanically induced electrical signals can enhance osteogenic differentiation.

The selected PEDOT:PSS concentration of 0.15% w/v was based on the existing literature and the specific requirements of our study. Previous studies reported on the utilization of PEDOT:PSS concentrations ranging from 0.1% to 0.3% w/v.[57] It is well-documented that PEDOT:PSS, when used at concentrations exceeding 0.2%, can exhibit cytotoxic effects.[58] Conversely, concentrations below 0.1% w/v have been shown to lack an effect on cell proliferation and differentiation. PVA/Gel control scaffolds were employed to determine whether the lack of PEDOT:PSS affects the osteogenic differentiation potential of pre-osteoblasts. Glutaraldehyde was used as crosslinker to covalently bind the free amino groups of gelatin and the hydroxyl groups of PVA, while GOPS was employed to crosslink PEDOT:PSS. As evident from the biological evaluation, the 2% v/v GOPS and the 0.025% v/v glutaraldehyde did not adversely affect the cell growth and differentiation potential. Similar concentrations of the crosslinkers have been reported in the literature.[12,28] Lyophilization was utilized for the fabrication of the scaffolds, enabling the formation of both large and small pores. Moreover, lyophilization served the purpose of an additional crosslinking method[59] inducing significant improvement in the flexibility and porosity of the scaffolds.

The FTIR and Raman spectral analysis of the scaffolds shows similar characteristic peaks with those of their base constituents, confirming successful integration. PVA/Gel scaffolds demonstrated the highest degradation/dissolution rates, which can be attributed to the liquid state of gelatin in cell culture conditions. Consequently, during incubation at 37 °C, the gelatin part of the scaffolds gradually dissolved as the melting point of gelatin is in the range of 35–40 °C. On the other hand, PEDOT:PSS-containing scaffolds appear to have significantly lower degradation/dissolution rates, which may be attributed to their reshaping and enhancement of mechanical properties due to their subjection to freezing-thawing cycles.[60] Structural changes within the PEDOT:PSS polymer involve the rearrangement of its molecular structure and the formation of new bonds, which contribute to improved integrity and enhanced mechanical properties.[27] PEDOT:PSS-containing scaffolds retained their integrity over 21 days in culture without noticeable morphological changes, holding particular significance for load-bearing areas. When scaffolds swell, their pore size increase, which can enhance cell attachment and migration, but can adversely affect their mechanical properties.[61] PVA/Gel/PEDOT scaffolds demonstrated improved water uptake

compared to PVA/Gel scaffolds. Non-significant differences were observed among them. Swelling behavior, ranging between 327 ± 29% for PVA/Gel/PEDOT and 266 ± 58% for the control PVA/Gel scaffold, affects the scaffolds' 3D structure and mechanical strength. Concerning the conductivity of scaffolds, existing literature[57] reports that increasing PEDOT:PSS concentration, from 0.1 to 0.3% w/v, results in increased electrical conductivity levels. It is evident that the scaffold type composed by PVA/Gel (0% PEDOT:PSS) exhibits the lowest conductivity, while the PEDOT:PSS-containing scaffolds exhibit the highest conductivity as evident by the static conductivity σ_0 results derived from dielectric measurements in both low and high frequency regions. The conductivity exponent for the high frequency regime is close to 1, indicating ohmic conduction. Comparison of the measured values with the ones on similar scaffolds shown in ref. 12 and 62 denotes much higher conductivity (factor from 3 to 8 for low frequency, that is the regime of interest for applications), that however could be explained by the different hydration conditions of hydrogels. Comparison with scaffolds from ref. 57 also shows higher values (factor from 1.5 to 5 for low frequency). Conclusively, the developed PVA/Gel/PEDOT:PSS scaffolds were engineered to impart electroconductivity within the 3D matrix, supporting cell signaling and mechanotransduction. Conductivity measurements were performed in a hydrated state to better approximate physiological conditions. With native bone displaying low intrinsic conductivity ($\sim 10^{-4}$–10^{-3} S m^{-1} for cortical bone),[63] the scaffolds, particularly those with higher PEDOT:PSS content, achieved values within this physiologically relevant range. Such conductivity levels are sufficient to promote cellular responses, including calcium signaling and osteogenic differentiation. The combined application of electrical and mechanical stimulation to more closely replicate the native bone microenvironment could be subject of another study. An additional aspect concerns the long-term preservation of the electroconductive properties. A relevant study by Guex *et al.*[12] reported that PEDOT:PSS scaffolds crosslinked with GOPS and doped with 4-dodecylbenzenesulfonic acid (DBSA) exhibited an initial decrease in conductivity after 4 days of incubation in serum, which was attributed to the burst release of the secondary dopant. Importantly, after this initial drop, the conductivity remained stable over 28 days of culture ($\sigma = 1.4 \pm 0.5 \times 10^{-4}$ for day 0, $2.0 \pm 1.5 \times 10^{-5}$ for day 4, and $6.1 \pm 4.0 \times 10^{-6}$ S cm^{-1} for day 28) without further statistically significant decline. This finding is particularly relevant since those scaffolds, similar to the ones developed here, were crosslinked with GOPS, suggesting that the conductivity of such systems, after the initial hydration period, remains relatively stable during culture conditions. However, long-term monitoring of scaffold electroconductivity during degradation remains essential to assess the stability of their electroactive properties under physiological conditions. Natural bone has internal pores, known as voids, with their volume referred to as porosity. Porosity determines permeability, allowing for nutrients and oxygen exchange, waste removal, and the ingrowth of bone tissue and blood vessels.[64] Notably, PEDOT:PSS-containing scaffolds exhibited the highest surface porosity compared to control scaffolds, accentuating their advantages. This may be attributed to the fabrication protocol. According to previous reports, freeze–thaw cycles as a post-synthesis physical process can reform the microstructure of conductive polymer hydrogels from clustered nanoparticles to interconnected nanosheets, leading to increased porosity, as well as to enhancement of mechanical and electrochemical properties.[27] In general, the surface porosity of the developed scaffolds does not exceed 35%, which is similar with other studies on freeze-dried and cross-linked scaffolds for tissue engineering,[65] while in hydrated state they exhibited higher porosity values. Tuning the preparation parameters such as the concentrations of the hydrogel components, the molecular weight of the polymer, and the crosslinking degree, affects the porosity, and lowering them could lead to scaffolds with higher porosity values of 70–85%, close to those of cancellous bone.[60] However, porosity was assessed from cross-sectional SEM images, providing information on surface porosity, whereas more comprehensive methods such as micro-CT would be required to accurately determine the overall scaffold architecture. In the context of mechanical characterization, PVA/Gel/PEDOT scaffolds exhibited superior elasticity compared to the PVA/Gel control scaffold. Previous studies have indicated that PVA/gelatin hydrogels typically exhibit a Young modulus of approximately 40–300 kPa.[66] In the present study, PVA/Gel/PEDOT scaffolds present 2.7 ± 0.4 MPa, exceeding the reported values. The significantly higher Young's modulus values can be attributed to the dual crosslinking[12,28] and lyophilization-induced structural rearrangements.[27] These factors contribute to an interconnected polymeric network, enhancing mechanical stability and elasticity. The measured stiffness of the developed scaffolds falls within the range of the cancellous bone, which exhibits a compressive strength of approximately 4–12 MPa, as previously reported.[67] Moreover, other studies have shown that substrates with stiffness in the low MPa or even kPa range optimally activate mechanotransduction pathways (*e.g.*, YAP/TAZ, Piezo1) and promote osteogenic differentiation of stem and progenitor cells.[68]

The cell morphology was evaluated visualizing the actin cytoskeletal structure, allowing for an assessment of cell shape and spreading. Cells on PVA/Gel scaffolds exhibited well-spread and organized actin filaments on day 1, while all scaffold types showed significant improvement in cell morphology on day 5. Cells on PVA/Gel/PEDOT scaffolds, in particular, displayed enhanced spreading and actin organization, suggesting improved cellular adaptation and proliferation over time. The cell adhesion patterns on the scaffolds were observed by visualization of vinculin, indicating areas of strong cell attachment. The control samples exhibited widespread and robust adhesion, while PEDOT-containing scaffolds showed varied adhesion patterns. However, by day 5, PVA/Gel/PEDOT scaffolds exhibited the highest levels of vinculin expression, suggesting improved cell adhesion over time. Cell viability and proliferation of pre-osteoblastic cells seeded onto the scaffolds demonstrated increasing cell numbers in

both hydrogel types. At day 7, PVA/Gel/PEDOT shows a significant growth compared to the control, signifying the positive effect of PEDOT:PSS on the cell number. The improved viability can be attributed to the electroconductive nature of PEDOT:PSS, that may stimulate cell–substrate interactions, thereby supporting early attachment and promoting proliferation over time. Related studies revealed dense extracellular matrix (ECM) deposition and increasing cell numbers over time, contributing to the formation of tissue-like structures by day 28.[12,62] Such observations confirm that PEDOT:PSS scaffolds not only support but actively promote the development of a biologically functional matrix over time.

Early bone healing phase is particularly sensitive to mechanical signals and lay the foundations for the entire repair process. In fact, it has been shown that allowing limited interfragmentary movement in the initial phase can enhance fracture healing in sheep models.[69] The compression of axial fracture that occurs as a result of weight bearing in experimental bone healing studies is reported between 10% and 33%,[70] and 2% and 20%,[71] in the fracture gaps for sheep and rat bone marrow, respectively. According to reported *in vivo* data and to previous studies investigating the effects of mechanical loading on cell differentiation, 5 and 10% of strain regimes were selected.[72,73] In order to mimic the load pattern in human movement, uniaxial compression at 1 Hz frequency was applied by means of a bioreactor.

The applied uniaxial mechanical stimulation demonstrated high cell viability in all scaffold types. However, the dynamic condition indicated higher number of dead cells on day 3, which can be attributed to the compression, that may stretch the cell membrane compromising cell survival. This observation is in line with previous studies, which have shown that mechanical stimulation at early time points—before the synthesis of sufficient extracellular matrix—can inhibit cell viability and cell cycle progression. In contrast, at later stages (*e.g.*, day 21), once the extracellular matrix is more established, mechanical stimulation has been reported to positively influence these parameters, supporting cell proliferation and tissue maturation.[74] The cellular response to external mechanical stimuli involves two processes, namely, mechanosensing and mechanotransduction.[75] Mechanosensing is the process by which cells sense physical signals from the extracellular environment through their mechanoreceptors. Cells then transduce the physical signals into biochemical signals. This process results in differentiation of the cells to specific lineages and is known as mechanotransduction.[76] Several typical mechanoreceptors are present on the membrane of MSCs and pre-osteoblastic cells such as integrins, mechanosensitive ion channels and primary cilia, making these cell types to sense and respond to mechanical stimulation. During bone formation, pre-osteoblastic cells sense external mechanical stimulation *via* mechanosensitive ion channels.[76] Mechanical stimulation modifies the conformation of mechanosensitive ion channels, generating an intracellular Ca^{2+} influx.[77] This influx leads to osteogenic differentiation and thereby to bone healing.[78] Additionally, the introduction of Ca^{2+} influences various targets, including calcium dependent YAP/TAZ, and can trigger osteogenic transcription.[77] YAP and TAZ are transcriptional cofactors considered important cellular mediators that define the cell fate, such as differentiation, proliferation or apoptosis.[79] An upregulation of calcium channel activation upon mechanical stimulation of cells within the scaffolds has been observed compared to static conditions. The presence of PEDOT:PSS amplified this effect, with PVA/Gel/PEDOT exhibiting the highest activation under both conditions, with the dynamic one being the most intense. This observation suggests that PEDOT:PSS facilitates a sustained activation of mechanosensitive calcium ion channels in pre-osteoblasts, such as Piezo1, even in the absence of external mechanical stimulation. A possible explanation is that the increased electrical conductivity and stiffness of the PVA/Gel/PEDOT scaffolds create a microenvironment that generates localized electrical or mechanical cues mimicking dynamic stimuli. Notably, a recent report[80] has shown that PEDOT:PSS substrates can directly enhance and sustain calcium ion influx by modulating membrane potential and promoting ion channel activation. These findings support the hypothesis that the PEDOT:PSS-containing scaffolds maintain calcium ion channels in a partially activated state under quiescent conditions, potentially priming cells for a rapid response to additional stimuli. Distinct patterns of YAP/TAZ distribution in cell-seeded scaffolds were also observed. Under mechanical stimulation, YAP/TAZ coactivators were primarily localized in the nuclei with high intensity, while in static conditions, they remained mainly in the cytoplasm with lower intensity. This nuclear translocation suggests the involvement of YAP/TAZ in mechanotransduction,[81] where mechanical forces trigger signaling pathways affecting gene expression and cellular behavior. The upregulation of YAP/TAZ in mechanically stimulated cells, compared to static controls, highlights their sensitivity to mechanical cues.

The ALP live staining method used in this study is specific for detecting the enzymatic activity of ALP within living cells. The confocal microscopy images demonstrate ALP activity patterns similar to previous reports.[50] PVA/Gel/PEDOT_D exhibits higher ALP activity at day 3, a trend continuing with lower intensity in the following time points, due to the early marker nature of ALP. Dynamic conditions consistently outperform the static ones. These observations are consistent with the biochemical ALP quantification results, which similarly demonstrated enhanced enzymatic activity under dynamic conditions, particularly in the PEDOT:PSS-containing scaffolds. The above findings are in line with the existing literature, which supports that PEDOT:PSS serves as an osteogenic differentiation stimulus for pre-osteoblastic cells.[12,82] Collagen and calcium deposition are both more pronounced under mechanical stimulation, especially in PVA/Gel/PEDOT_D. EDS analysis showed significant calcium and phosphorus deposition across diverse scaffolds. Particularly, at the early time point of day 7, calcium deposition was evident in PVA/Gel/PEDOT_D. By day 21, calcium and phosphorus deposition were widespread across all scaffold types. However, only PVA/Gel/PEDOT_D pre-

sented phosphorus at day 14. Similar results were evident in previous studies that showed the important role of PEDOT:PSS in biomineralization.[11,12] A Ca/P ratio of 1.66 for the PVA/Gel/PEDOT_D is close to that of hydroxyapatite. XRD analysis on the Ca and P deposition from the pre-osteoblasts cultures revealed that the mineral phase was poorly crystalline, which is typical for biological apatites.[53] Particularly, PVA/Gel/PEDOT_D exhibits sharp peaks at characteristic hydroxyapatite 2θ angles, indicating that apatite crystals grew with preferential orientations along the (211) and (222) crystallographic planes. Overall, these findings validate the osteogenic commitment of pre-osteoblasts when cultured on electroactive PEDOT:PSS-containing scaffolds under mechanical stimulation. Future work would complement these results by incorporating gene expression analyses of key osteogenic markers, thereby providing a more comprehensive understanding of the differentiation process.

The *in vivo* evaluation in a subcutaneous mouse model after two weeks revealed lack of any signs of foreign body reaction in any of the implanted scaffold types, validating their biocompatibility. The absence of immune recruitment and macrophage aggregation is consistent with the constructs' biocompatibility, confirming that they are well-received by the surrounding tissue. The implementation of orthotopic bone defect models would validate the regenerative performance of the developed scaffolds.

In order to provide insight for further optimization steps of this kind of scaffolds to obtain appropriate functions, the general question arises on how mechanical stimulation performed on a conductive material could be able to produce electrical cues to stimulate cellular growth or osteogenic differentiation. A possible mechanism could be put forward to comply with the observed effects. It seems well assessed that cell activity has a dependence on the redox state of the substrate. Works by the group of Malliaras[83] report on the production of PEDOT:TOS (*p*-toluenesulfonate) film stripes with varying redox state along their length, and demonstrate how cell activity is enhanced, in their case, only on the film in the oxidized state. A PEDOT:TOS stripe was prepared with a redox gradient along its length, and after cell proliferation, fluorescence micrographs of calcein-green stained 3T3-L1 cells evidenced their growth on the oxidized part of the substrate only. It should be remarked that these experiments were conducted without applying any electric potential during the cell proliferation experiments. It could be hypothesized that mechanical strain could somehow affect the electronic properties of the material. In a work by the group of Joo,[84] changes of the chemical environment (electronic binding energy) of the material are reported as the effect of mechanical strain. To this purpose, sulfur (S 2p) X-ray photoelectron spectroscopy (XPS) data were analyzed, on different PEDOT:PSS samples as a function of strain. To this purpose, PEDOT:PSS thin films were spin-coated onto polyimide (Kapton) substrates, previously surface-treated by air plasma to improve adhesion, and mechanically stretched up to the desired strain. The XPS energy distribution shifted to lower energy as the effect of strain, meaning that the required energy for detaching electrons decreased as the effect of the applied strain. In particular, the binding energy was shifted by 0.3 eV for a 16% strain. A similar mechanism could justify the production of the electrical cues sufficient to obtain noticeable biological effects like the ones reported here.

5. Conclusion

This study introduces novel electroactive and mechanoresponsive scaffolds composed of PEDOT:PSS, PVA, and gelatin, specifically designed to mimic the biomechanical and electrical environment of the native bone tissue. The scaffolds offer a promising platform for bone tissue engineering applications, where mechanical stimulation and electrical signaling play a synergistic role in cellular behavior and osteogenic differentiation. Under dynamic conditions, the PEDOT:PSS-containing scaffolds demonstrate enhanced biological performance, including elevated ALP activity, upregulated mechanosensitive calcium ion channel activity, and nuclear translocation of YAP/TAZ, all indicative of stimulated osteogenic differentiation. Notably, the PVA/Gel/PEDOT_D scaffolds showed the most favorable responses, confirming the hypothesis that mechanical stimulation of electroactive scaffolds can promote osteogenesis through the activation of mechanosensitive pathways. *In vivo* results confirmed the biocompatibility of the constructs, laying a foundation for future application in orthopedic regenerative medicine, while future work using an orthotopic bone defect model would be critical for assessing the functional bone healing capacity. In addition, a combination of electrical and mechanical stimulation of cell-loaded constructs would shed more light on the effect of the scaffold conductivity on the osteogenic cellular responses. Addressing these issues in future studies would contribute to unlock the translational potential of the developed biomimetic platform.

Conflicts of interest

The authors state that there is no conflict of interest.

Data availability

Data will be made available on request. Supplementary information (SI) is available. See DOI: https://doi.org/10.1039/d5bm01064k.

Acknowledgements

This research was funded by the Hellenic Foundation for Research and Innovation (H.F.R.I.) project number HFRI-FM17-1999. Thanks are due to Simone Capaccioli (University of Pisa) for sharing the dielectric spectrometry instrumentation through the CISUP network, and to

Margherita Montorsi and Lorenzo Scarpelli (CNR-IPCF) for interesting discussions and help with some of the measurements. We also acknowledge Dr Vassilis M. Papadakis and Dr George Kenanakis (FORTH) for providing support with Raman spectroscopy.

References

1 A. H. Schmidt, Autologous bone graft: Is it still the gold standard?, *Injury*, 2021, **52**, S18–S22.
2 Y. Zhang, D. Wu, X. Zhao, M. Pakvasa, A. B. Tucker, H. Luo, K. H. Qin, D. A. Hu, E. J. Wang, A. J. Li, M. Zhang, Y. Mao, M. Sabharwal, F. He, C. Niu, H. Wang, L. Huang, D. Shi, Q. Liu, N. Ni, K. Fu, C. Chen, W. Wagstaff, R. R. Reid, A. Athiviraham, S. Ho, M. J. Lee, K. Hynes, J. Strelzow, T. C. He and M. El Dafrawy, Stem Cell-Friendly Scaffold Biomaterials: Applications for Bone Tissue Engineering and Regenerative Medicine, *Front. Bioeng. Biotechnol.*, 2020, **8**, 598607.
3 M. Chatzinikolaidou, C. Pontikoglou, K. Terzaki, M. Kaliva, A. Kalyva, E. Papadaki, M. Vamvakaki and M. Farsari, Recombinant human bone morphogenetic protein 2 (rhBMP-2) immobilized on laser-fabricated 3D scaffolds enhance osteogenesis, *Colloids Surf., B*, 2017, **149**, 233–242.
4 B. Safari, S. Davaran and A. Aghanejad, Osteogenic potential of the growth factors and bioactive molecules in bone regeneration, *Int. J. Biol. Macromol.*, 2021, **175**, 544–557.
5 A. A. Bertrand, S. H. Malapati, D. T. Yamaguchi and J. C. Lee, The Intersection of Mechanotransduction and Regenerative Osteogenic Materials, *Adv. Healthcare Mater.*, 2020, **9**(20), 2000709.
6 B. P. Hung, D. L. Hutton and W. L. Grayson, Mechanical control of tissue-engineered bone, *Stem Cell Res. Ther.*, 2013, **4**(1), 10.
7 J. Wolff, *Das gestetz der transformation der knochem*, Verlag von August Hirschwald, 1892.
8 S. R. Pollack, Bioelectrical Properties of Bone: Endogenous Electrical Signals, *Orthop. Clin. North Am.*, 1984, **15**(1), 3–14.
9 J. Sun, W. Xie, Y. Wu, Z. Li and Y. Li, Accelerated Bone Healing via Electrical Stimulation, *Adv. Sci.*, 2024, 2404190.
10 L. Wang, Y. Pang, Y. Tang, X. Wang, D. Zhang, X. Zhang, Y. Yu, X. Yang and Q. Cai, A biomimetic piezoelectric scaffold with sustained Mg^{2+} release promotes neurogenic and angiogenic differentiation for enhanced bone regeneration, *Bioact. Mater.*, 2023, **25**, 399–414.
11 M. Yazdimamaghani, M. Razavi, M. Mozafari, D. Vashaee, H. Kotturi and L. Tayebi, Biomineralization and biocompatibility studies of bone conductive scaffolds containing poly (3,4-ethylenedioxythiophene):poly(4-styrene sulfonate) (PEDOT:PSS), *J. Mater. Sci.: Mater. Med.*, 2015, **26**(12), 274.
12 A. G. Guex, J. L. Puetzer, A. Armgarth, E. Littmann, E. Stavrinidou, E. P. Giannelis, G. G. Malliaras and M. M. Stevens, Highly porous scaffolds of PEDOT:PSS for bone tissue engineering, *Acta Biomater.*, 2017, **62**, 91–101.
13 P. B. Kasi, A. Serafin, L. O'Brien, N. Moghbel, L. N. Novikov, P. Kelk and M. N. Collins, Electroconductive gelatin/hyaluronic acid/hydroxyapatite scaffolds for enhanced cell proliferation and osteogenic differentiation in bone tissue engineering, *Biomater. Adv.*, 2025, **173**, 214286.
14 C. Adler, M. Monavari, G. A. Abraham, A. R. Boccaccini and F. Ghorbani, Mussel-inspired polydopamine decorated silane modified-electroconductive gelatin-PEDOT:PSS scaffolds for bone regeneration, *RSC Adv.*, 2023, **13**(23), 15960–15974.
15 F. Ghorbani, B. Ghalandari, M. Sahranavard, A. Zamanian and M. N. Collins, Tuning the biomimetic behavior of hybrid scaffolds for bone tissue engineering through surface modifications and drug immobilization, *Mater. Sci. Eng., C*, 2021, **130**, 112434.
16 X. Yang, Y. Jia, K. Yao, Y. Wang and J. Ma, A study on piezoelectric effect of gelatin gel, *J. Appl. Polym. Sci.*, 1996, **62**(13), 2351–2354.
17 I. Lukin, I. Erezuma, L. Maeso, J. Zarate and M. F. Desimone, Progress in Gelatin as Biomaterial for Tissue Engineering, *Pharmaceutics*, 2022, **14**(6), 1177.
18 A. Kumar and S. S. Han, PVA-based hydrogels for tissue engineering: A review, *Int. J. Polym. Mater. Polym. Biomater.*, 2017, **66**(4), 159–182.
19 M. G. Cascone, L. Lazzeri, E. Sparvoli, M. Scatena, L. P. Serino and S. Danti, Morphological evaluation of bioartificial hydrogels as potential tissue engineering scaffolds, *J. Mater. Sci.: Mater. Med.*, 2004, **15**(12), 1309–1313.
20 Y. Hou, W. Xie, K. Achazi, J. L. Cuellar-Camacho, M. F. Melzig, W. Chen and R. Haag, Injectable degradable PVA microgels prepared by microfluidic technology for controlled osteogenic differentiation of mesenchymal stem cells, *Acta Biomater.*, 2018, **77**, 28–37.
21 H. M. Frost, Perspectives: bone's mechanical usage windows, *Bone Miner.*, 1992, **19**(3), 257–271.
22 D. Kaspar, W. Seidl, C. Neidlinger-Wilke, A. Beck, L. Claes and A. Ignatius, Proliferation of human-derived osteoblast-like cells depends on the cycle number and frequency of uniaxial strain, *J. Biomech.*, 2002, **35**(7), 873–880.
23 F. Barbosa, F. F. F. Garrudo, A. C. Marques, J. M. S. Cabral, J. Morgado, F. C. Ferreira and J. C. Silva, Novel Electroactive Mineralized Polyacrylonitrile/PEDOT:PSS Electrospun Nanofibers for Bone Repair Applications, *Int. J. Mol. Sci.*, 2023, **24**(17), 13203.
24 J. C. Silva, P. Marcelino, J. Meneses, F. Barbosa, C. S. Moura, A. C. Marques, J. M. S. Cabral, P. Pascoal-Faria, N. Alves, J. Morgado, F. C. Ferreira and F. F. F. Garrudo, Synergy between 3D-extruded electroconductive scaffolds and electrical stimulation to improve bone tissue engineering strategies, *J. Mater. Chem. B*, 2024, **12**(11), 2771–2794.
25 D. D'Alessandro, C. Ricci, M. Milazzo, G. Strangis, F. Forli, G. Buda, M. Petrini, S. Berrettini, M. J. Uddin, S. Danti and

P. Parchi, Piezoelectric Signals in Vascularized Bone Regeneration, *Biomolecules*, 2021, **11**(11), 1731.

26 A. R. Spencer, A. Primbetova, A. N. Koppes, R. A. Koppes, H. Fenniri and N. Annabi, Electroconductive Gelatin Methacryloyl-PEDOT:PSS Composite Hydrogels: Design, Synthesis, and Properties, *ACS Biomater. Sci. Eng.*, 2018, **4**(5), 1558–1567.

27 W. Li, H. Lu, N. Zhang and M. Ma, Enhancing the Properties of Conductive Polymer Hydrogels by Freeze–Thaw Cycles for High-Performance Flexible Supercapacitors, *ACS Appl. Mater. Interfaces*, 2017, **9**(23), 20142–20149.

28 A. P. McGuigan and M. V. Sefton, Modular tissue engineering: fabrication of a gelatin-based construct, *J. Tissue Eng. Regen. Medicine*, 2007, **1**(2), 136–145.

29 H. D. G. Hedderich, Thermo-Nicolet 6700 Series FTIR User's Guide, 9/6/2023. https://www.chem.purdue.edu/ric/docs/6700-FTIR-3.0-handout.pdf.

30 D. Lee, H. Zhang and S. Ryu, Elastic Modulus Measurement of Hydrogels, in *Cellulose-Based Superabsorbent Hydrogels*, ed. M. I. H. Mondal, Springer International Publishing, Cham, 2018, pp. 1–21.

31 G.-I. Kontogianni, K. Loukelis, A. F. Bonatti, E. Batoni, C. De Maria, R. Naseem, K. Dalgarno, G. Vozzi, D. B. MacManus, S. Mondal, N. Dunne, C. Vitale-Brovarone and M. Chatzinikolaidou, Effect of Uniaxial Compression Frequency on Osteogenic Cell Responses in Dynamic 3D Cultures, *Bioengineering*, 2023, **10**(5), 532.

32 G.-I. Kontogianni, K. Loukelis, A. F. Bonatti, E. Batoni, C. De Maria, G. Vozzi, R. Naseem, K. Dalgarno, H. Shin, C. Vitale-Brovarone and M. Chatzinikolaidou, A Mechanically Stimulated Co-culture in 3-Dimensional Composite Scaffolds Promotes Osteogenic and Anti-osteoclastogenic Activity and M2 Macrophage Polarization, *Biomater. Res.*, 2025, **29**, 0135.

33 S. Vimalraj, Alkaline phosphatase: Structure, expression and its function in bone mineralization, *Gene*, 2020, **754**, 144855.

34 E. Batoni, N. N. Tavernaraki, V. Platania, C. De Maria, M. Chatzinikolaidou and G. Vozzi, 3D printed osteoporotic bone model validated in dynamic culture, *Bioprinting*, 2025, **48**, e00410.

35 F. J. Geissel, V. Platania, N. DeBerardinis, C. Skjöldebrand, G. N. Belibasakis, C. Persson, G. Hulsart-Billström, M. Chatzinikolaidou and G. A. Sotiriou, Nanostructured Ag-Bioglass Implant Coatings with Antibacterial and Osteogenic Activity, *Adv. Mater. Interfaces*, 2023, **10**(3), 2201980.

36 L. Rittié, Method for Picrosirius Red-Polarization Detection of Collagen Fibers in Tissue Sections, *Methods Mol. Biol.*, 2017, **1627**, 395–407.

37 M. A. El-Meligy, K. Valachová, I. Juránek, T. M. Tamer and L. Šoltés, Preparation and Physicochemical Characterization of Gelatin-Aldehyde Derivatives, *Molecules*, 2022, **27**(20), 7003.

38 K. Loukelis, D. Papadogianni and M. Chatzinikolaidou, Kappa-carrageenan/chitosan/gelatin scaffolds enriched with potassium chloride for bone tissue engineering, *Int. J. Biol. Macromol.*, 2022, **209**, 1720–1730.

39 H. Hu, J. H. Xin, H. Hu, A. Chan and L. He, Glutaraldehyde–chitosan and poly (vinyl alcohol) blends, and fluorescence of their nano-silica composite films, *Carbohydr. Polym.*, 2013, **91**(1), 305–313.

40 N. M. Sadiq, S. B. Aziz and M. F. Z. Kadir, Development of Flexible Plasticized Ion Conducting Polymer Blend Electrolytes Based on Polyvinyl Alcohol (PVA): Chitosan (CS) with High Ion Transport Parameters Close to Gel Based Electrolytes, *Gels*, 2022, **8**(3), 153.

41 N. Kanjana, W. Maiaugree, P. Laokul, I. Chaiya, T. Lunnoo, P. Wongjom, Y. Infahsaeng, B. Thongdang and V. Amornkitbamrung, Fly ash boosted electrocatalytic properties of PEDOT:PSS counter electrodes for the triiodide reduction in dye-sensitized solar cells, *Sci. Rep.*, 2023, **13**(1), 6012.

42 Ö. Yağci and O. K. Özdemir, Improving the electrical conductivity and electrochemical properties of PEDOT:PSS thin films by Ca and Mg doping, *Polym. Bull.*, 2022, **79**(12), 11493–11509.

43 A. A. Farah, S. A. Rutledge, A. Schaarschmidt, R. Lai, J. P. Freedman and A. S. Helmy, Conductivity enhancement of poly(3,4-ethylenedioxythiophene)-poly(styrenesulfonate) films post-spincasting, *J. Appl. Phys.*, 2012, **112**(11).

44 F. Alihosseini, 10 – Plant-based compounds for antimicrobial textiles, in *Antimicrobial Textiles*, ed. G. Sun, Woodhead Publishing, 2016, pp. 155–195.

45 M. Wiśniewska, V. Bogatyrov, I. Ostolska, K. Szewczuk-Karpisz, K. Terpiłowski and A. Nosal-Wiercińska, Impact of poly(vinyl alcohol) adsorption on the surface characteristics of mixed oxide MnxOy–SiO_2, *Adsorption*, 2016, **22**(4), 417–423.

46 P. M. Smith, I. Sutradhar, M. Telmer, R. Magar, A. B. Farimani and B. Reeja-Jayan, Isolating Specific vs. Non-Specific Binding Responses in Conducting Polymer Biosensors for Bio-Fingerprinting, *Sensors*, 2021, **21**(19), 6335.

47 A. Håkansson, S. Han, S. Wang, J. Lu, S. Braun, M. Fahlman, M. Berggren, X. Crispin and S. Fabiano, Effect of (3-glycidyloxypropyl)trimethoxysilane (GOPS) on the electrical properties of PEDOT:PSS films, *J. Polym. Sci., Polym. Phys.*, 2017, **55**(10), 814–820.

48 P. M. A. Alves, R. A. Carvalho, I. C. F. Moraes, C. G. Luciano, A. M. Q. B. Bittante and P. J. A. Sobral, Development of films based on blends of gelatin and poly (vinyl alcohol) cross linked with glutaraldehyde, *Food Hydrocolloids*, 2011, **25**(7), 1751–1757.

49 K. J. Andrew, Dielectric relaxation in solids, *J. Phys. D: Appl. Phys.*, 1999, **32**(14), R57.

50 M. Ahmad, T. Kroll, J. Jakob, A. Rauch, A. Ploubidou and J. Tuckermann, Cell-based RNAi screening and high-content analysis in primary calvarian osteoblasts applied to identification of osteoblast differentiation regulators, *Sci. Rep.*, 2018, **8**(1), 14045.

51 W. Florkiewicz, D. Słota, A. Placek, K. Pluta, B. Tyliszczak, T. E. L. Douglas and A. Sobczak-Kupiec, Synthesis and

Characterization of Polymer-Based Coatings Modified with Bioactive Ceramic and Bovine Serum Albumin, *J. Funct. Biomater.*, 2021, **12**(2), 21.

52 S. Lara-Ochoa, W. Ortega-Lara and C. E. Guerrero-Beltrán, Hydroxyapatite Nanoparticles in Drug Delivery: Physicochemistry and Applications, *Pharmaceutics*, 2021, **13**(10), 1642.

53 W. N. Addison, V. Nelea, F. Chicatun, Y. C. Chien, N. Tran-Khanh, M. D. Buschmann, S. N. Nazhat, M. T. Kaartinen, H. Vali, M. M. Tecklenburg, R. T. Franceschi and M. D. McKee, Extracellular matrix mineralization in murine MC3T3-E1 osteoblast cultures: An ultrastructural, compositional and comparative analysis with mouse bone, *Bone*, 2015, **71**, 244–256.

54 J. Jeong, J. H. Kim, J. H. Shim, N. S. Hwang and C. Y. Heo, Bioactive calcium phosphate materials and applications in bone regeneration, *Biomater. Res.*, 2019, **23**(1), 4.

55 R. B. Borgens, Endogenous ionic currents traverse intact and damaged bone, *Science*, 1984, **225**(4661), 478–482.

56 M. Janmohammadi, M. S. Nourbakhsh, M. Bahraminasab and L. Tayebi, Enhancing bone tissue engineering with 3D-Printed polycaprolactone scaffolds integrated with tragacanth gum/bioactive glass, *Mater. Today Bio*, 2023, **23**, 100872.

57 A. Shahini, M. Yazdimamaghani, K. J. Walker, M. A. Eastman, H. Hatami-Marbini, B. J. Smith, J. L. Ricci, S. V. Madihally, D. Vashaee and L. Tayebi, 3D conductive nanocomposite scaffold for bone tissue engineering, *Int. J. Nanomed.*, 2014, **9**, 167–181.

58 P. Bhattacharjee and M. Ahearne, Fabrication and Biocompatibility of Electroconductive Silk Fibroin/PEDOT:PSS Composites for Corneal Epithelial Regeneration, *Polymers*, 2020, **12**(12), 3028.

59 W. X. Waresindo, H. R. Luthfianti, A. Priyanto, D. A. Hapidin, D. Edikresnha, A. H. Aimon, T. Suciati and K. Khairurrijal, Freeze–thaw hydrogel fabrication method: basic principles, synthesis parameters, properties, and biomedical applications, *Mater. Res. Express*, 2023, **10**(2), 024003.

60 J. I. Dawson, J. M. Kanczler, X. B. Yang, G. S. Attard and R. O. Oreffo, Clay gels for the delivery of regenerative microenvironments, *Adv. Mater.*, 2011, **23**(29), 3304–3308.

61 C. Shi, X. Hou, D. Zhao, H. Wang, R. Guo and Y. Zhou, Preparation of the bioglass/chitosan-alginate composite scaffolds with high bioactivity and mechanical properties as bone graft materials, *J. Mech. Behav. Biomed. Mater.*, 2022, **126**, 105062.

62 F. Furlani, E. Campodoni, N. Sangiorgi, M. Montesi, A. Sanson, M. Sandri and S. Panseri, Electroconductive scaffolds based on gelatin and PEDOT:PSS for cardiac regeneration, *Int. J. Biol. Macromol.*, 2023, **224**, 266–280.

63 T. W. Balmer, S. Vesztergom, P. Broekmann, A. Stahel and P. Büchler, Characterization of the electrical conductivity of bone and its correlation to osseous structure, *Sci. Rep.*, 2018, **8**(1), 8601.

64 A. Teimouri, S. Roohafza, M. Azadi and A. N. Chermahini, Fabrication and characterization of chitosan/gelatin/nano-diopside composite scaffolds for tissue engineering application, *Polym. Bull.*, 2018, **75**(4), 1487–1504.

65 A. Autissier, C. L. Visage, C. Pouzet, F. Chaubet and D. Letourneur, Fabrication of porous polysaccharide-based scaffolds using a combined freeze-drying/cross-linking process, *Acta Biomater.*, 2010, **6**(9), 3640–3648.

66 H. Kim, G. H. Yang and G. Kim, Three-dimensional gelatin/PVA scaffold with nanofibrillated collagen surface for applications in hard-tissue regeneration, *Int. J. Biol. Macromol.*, 2019, **135**, 21–28.

67 M. Milazzo, N. Contessi Negrini, S. Scialla, B. Marelli, S. Farè, S. Danti and M. J. Buehler, Additive Manufacturing Approaches for Hydroxyapatite-Reinforced Composites, *Adv. Funct. Mater.*, 2019, **29**(35), 1903055.

68 A. J. Engler, S. Sen, H. L. Sweeney and D. E. Discher, Matrix Elasticity Directs Stem Cell Lineage Specification, *Cell*, 2006, **126**(4), 677–689.

69 P. Klein, H. Schell, F. Streitparth, M. Heller, J. P. Kassi, F. Kandziora, H. Bragulla, N. P. Haas and G. N. Duda, The initial phase of fracture healing is specifically sensitive to mechanical conditions, *J. Orthop. Res.*, 2003, **21**(4), 662–669.

70 H. Schell, M. S. Thompson, H. J. Bail, J. E. Hoffmann, A. Schill, G. N. Duda and J. Lienau, Mechanical induction of critically delayed bone healing in sheep: radiological and biomechanical results, *J. Biomech.*, 2008, **41**(14), 3066–3072.

71 B. S. Klosterhoff, K. G. Ong, L. Krishnan, K. M. Hetzendorfer, Y. H. Chang, M. G. Allen, R. E. Guldberg and N. J. Willett, Wireless Implantable Sensor for Noninvasive, Longitudinal Quantification of Axial Strain Across Rodent Long Bone Defects, *J. Biomech. Eng. – Trans. ASME*, 2017, **139**(11), 1110041–1110048.

72 C. Liu, R. Abedian, R. Meister, C. Haasper, C. Hurschler, C. Krettek, G. von Lewinski and M. Jagodzinski, Influence of perfusion and compression on the proliferation and differentiation of bone mesenchymal stromal cells seeded on polyurethane scaffolds, *Biomaterials*, 2012, **33**(4), 1052–1064.

73 A. Sittichokechaiwut, J. H. Edwards, A. M. Scutt and G. C. Reilly, Short bouts of mechanical loading are as effective as dexamethasone at inducing matrix production by human bone marrow mesenchymal stem cell, *Eur. Cells Mater.*, 2010, **20**, 45–57.

74 C. Huselstein, N. de Isla, M. N. Kolopp-Sarda, H. Kerdjoudj, S. Muller and J. F. Stoltz, Influence of mechanical stress on cell viability, *Biorheology*, 2006, **43**(3,4), 371–375.

75 C. Loebel, R. L. Mauck and J. A. Burdick, Local nascent protein deposition and remodelling guide mesenchymal stromal cell mechanosensing and fate in three-dimensional hydrogels, *Nat. Mater.*, 2019, **18**(8), 883–891.

76 R. M. Delaine-Smith and G. C. Reilly, Chapter Twenty - The Effects of Mechanical Loading on Mesenchymal Stem Cell

Differentiation and Matrix Production, in *Vitamins & Hormones*, ed. G. Litwack, Academic Press, 2011, pp. 417–480.

77 J. S. LaGuardia, K. Shariati, M. Bedar, X. Ren, S. Moghadam, K. X. Huang, W. Chen, Y. Kang, D. T. Yamaguchi and J. C. Lee, Convergence of Calcium Channel Regulation and Mechanotransduction in Skeletal Regenerative Biomaterial Design, *Adv. Healthcare Mater.*, 2023, **12**(27), 2301081.

78 C. Shuai, W. Yang, S. Peng, C. Gao, W. Guo, Y. Lai and P. Feng, Physical stimulations and their osteogenesis-inducing mechanisms, *Int. J. Bioprint.*, 2018, **4**(2), 138.

79 G. Zhong, S. Su, J. Li, H. Zhao, D. Hu, J. Chen, S. Li, Y. Lin, L. Wen, X. Lin, G. Xian, D. Xu and Q. Zeng, Activation of Piezo1 promotes osteogenic differentiation of aortic valve interstitial cell through YAP-dependent glutaminolysis, *Sci. Adv.*, 2023, **9**(22), eadg0478.

80 Y. Guo, S. Ma, D. Wang, F. Mei, Y. Guo, B. C. Heng, S. Zhang, Y. Huang, Y. Wei, Y. He, W. Liu, M. Xu, X. Zhang, L. Chen and X. Deng, HtrA3 paves the way for MSC migration and promotes osteogenesis, *Bioact. Mater.*, 2024, **38**, 399–410.

81 K. E. Scott, S. I. Fraley and P. Rangamani, Transfer function for YAP/TAZ nuclear translocation revealed through spatial systems modeling, bioRxiv, 2020, DOI: doi.org/10.1101/2020.10.14.340349.

82 N. Fani, M. Hajinasrollah, M. Asghari Vostikolaee, M. Baghaban Eslaminejad, F. Mashhadiabbas, N. Tongas, M. Rasoulianboroujeni, A. Yadegari, K. Ede, M. Tahriri and L. Tayebi, Influence of conductive PEDOT:PSS in a hard tissue scaffold: In vitro and in vivo study, *J. Bioact. Compat. Polym.*, 2019, **34**(6), 436–441.

83 A. M. D. Wan, D. J. Brooks, A. Gumus, C. Fischbach and G. G. Malliaras, Electrical control of cell density gradients on a conducting polymer surface, *Chem. Commun.*, 2009, (35), 5278–5280.

84 Y.-Y. Lee, G. M. Choi, S.-M. Lim, J.-Y. Cho, I.-S. Choi, K. T. Nam and Y.-C. Joo, Growth Mechanism of Strain-Dependent Morphological Change in PEDOT:PSS Films, *Sci. Rep.*, 2016, **6**(1), 25332.

